Astronomy & Astrophysics manuscript no. 7655tex
February 1, 2008

© ESO 2008

arXiv:0709.0859v1 [astro-ph] 6 Sep 2007

SNLS Spectroscopy: Testing for Evolution in Type Ia Supernovae

T. J. Bronder[1,⋆⋆⋆], I. M. Hook[1], P. Astier[2], D. Balam[3], C. Balland[2], S. Basa[4], R. G. Carlberg[5], A. Conley[5], D. Fouchez[6], J. Guy[2], D. A. Howell[5], J. D. Neill[7], R. Pain[2], K. Perrett[5], C. J. Pritchet[3], N. Regnault[2], M. Sullivan[5], S. Baumont[2], S. Fabbro[8], M. Filliol[9], S. Perlmutter[10], and P. Ripoche[6]

[1] University of Oxford Astrophysics, Denys Wilkinson Building, Keble Road, Oxford OX1 3RH, UK
[2] LPNHE, CNRS-IN2P3 and University of Paris VI & VII, 75005 Paris, France
[3] Department of Physics and Astronomy, University of Victoria, PO Box 3055, Victoria, BC V8W 3P6, Canada
[4] LAM, BP8, Traverse du Siphon, 13376 Marseille Cedex 12, France
[5] Department of Astronomy and Astrophysics, University of Toronto, 50 St. George Street, Toronto, ON M5S 3H4, Canada
[6] CPPM, CNRS-Luminy, Case 907, 13288 Marseille Cedex 9, France
[7] SRL California Institute of Technology, 1200 East California Blvd. , Pasadena CA 91125
[8] CENTRA - Centro Multidisciplinar de Astrofísica, IST, Avenida Rovisco Pais, 1049 Lisbon, Portugal
[9] LAM CNRS, BP8, Traverse du Siphon, 13376 Marseille Cedex 12, France
[10] University of California, Berkeley and Lawrence Berkeley National Laboratory, Mail Stop 50-232, Lawrence Berkeley National Laboratory, 1 Cyclotron Road, Berkeley CA 94720 USA

Received ; accepted

ABSTRACT

Aims. We present a quantitative study of a new data set of high redshift Type Ia supernovae spectra, observed at the Gemini telescopes during the first 34 months of the Supernova Legacy Survey. During this time 123 supernovae candidates were observed, of which 87 have been identified as SNe Ia at a median redshift of $z = 0.720$. Spectra from the entire second year of the survey and part of the third year (59 total SNe candidates with 46 confirmed SNe Ia) are published here for the first time. The spectroscopic measurements made on this data set are used determine if these distant SNe comprise a population similar to those observed locally.
Methods. Rest-frame equivalent width and ejection velocity measurements are made on four spectroscopic features. Corresponding measurements are presented for a set of 167 spectra from 24 low-z SNe Ia from the literature.
Results. We show that there exists a sample at high redshift with properties similar to nearby SNe. The high-z measurements are consistent with the range of measurements at low-z and no significant difference was found between the distributions of measurements at low and high redsift for three of the features. The fourth feature displays a possible difference that should be investigated further. Correlations between Type Ia SNe properties and host galaxy morphology were also found to be similar at low and high z, and within each host galaxy class we see no evidence for redshift-evolution in SN properties. A new correlation between SNe Ia peak magnitude and the equivalent width of SiII absorption is presented. Tests on a sub-set of the SNLS SNe demonstrates that this correlation reduces the scatter in SNe Ia luminosity distances in a manner consistent with the lightcurve shape-luminosity corrections that are used for Type Ia SNe cosmology.
Conclusions. We show that this new sample of SNLS SNe Ia has spectroscopic properties similar to nearby objects.

Key words. supernovae: general - cosmology: observations - surveys

1. Introduction

Hubble diagrams making use of the 'standardizeable' nature of Type Ia SNe (Riess *et al.* 1998; Perlmutter *et al.* 1999; Knop *et al.* 2003; Astier *et al.* 2006) indicate the significant presence of a 'dark energy' that is driving the accelerating expansion of the universe. This result is additionally constrained by observations of the power spectrum of the cosmic microwave backround (Spergel *et al.* 2003, 2006), properties of massive clusters (Allen, Schmidt & Fabian 2002) and other large scale structure observations (Seljak *et al.* 2005). The equation of state parameter of this dark energy (defined as $w = p/\rho$, the ratio of dark energy pressure p to density ρ) has been investigated by recent surveys (Knop *et al.* 2003; Barris *et al.* 2004; Riess *et al.* 2004), but the results are still consistent with a wide range of dark energy models. The CFHT Supernova Legacy Survey [SNLS, Astier *et al.* (2006)] aims to increase the measured precision of this parameter by finding and following about 500 distant Type Ia SNe over a five-year survey lifetime.

The fundamental assumptions of the methods used to estimate the cosmological parameters with SNe are that the selected low-z and high-z objects have similar peak magnitudes (*i.e.* within the locally observed dispersion) and that the established lightcurve shape-luminosity relations are applicable to these SNe at all redshifts. However, the current understanding of SNe Ia explosions [see Hillebrandt & Niemeyer (2000) for a review] and their progenitors (PGs) illustrates that there may be some differences, or evolution, in their inherent properties at high redshifts (Hoflich et al 1998, Hatano et al 2000, Lentz et al 2000). Such effects could distort the cosmological results of SNe Ia surveys. The differences in properties of SNe in hosts of different morphology (Wang *et al.* 1997; Umeda *et al.* 1999; Hamuy *et al.* 2000; Howell 2001;

Send offprint requests to: T. J. Bronder

⋆ The Figures in Appendix A are only available in electronic form via http://www.edpsciences/anada.org

⋆⋆ E-mail:jtb@astro.ox.ac.uk, current address: AFRL Directed Energy 3550 Aberdeen Ave SE, Kirtland AFB, Albuquerque, NM 87117

Sullivan *et al.* 2003; Gallagher *et al.* 2005; Sullivan *et al.* 2006) provides additional evidence of SNe Ia heterogeneity. The luminosity-lightcurve shape calibrations used for SNe Ia cosmology (Riess, Press, & Kirshner 1996; Phillips *et al.* 1999; Goldhaber *et al.* 2001; Guy *et al.* 2005) make an empirical accomodation for the dispersion of SNe properties observed locally, but these methods may be vulnerable to systematic changes in the SNe Ia population at high redshifts (Leibundgut 2001). Thus, it is imperative to undertake a quantitative investigation to determine whether there are any changes in these objects that may affect their reliability as distance indicators for cosmology.

The spectra of SNe Ia reveal more subtle characteristics than photometric observations and are well suited for this investigation. For example, measurements of photospheric ejection velocities ($v_{\rm ej}$) explore the kinetic energy and distribution of elements in the expanding SN ejecta. These measurements provided some of the first evidence of intrinsic differences between Type Ia SNe (Branch *et al.* 1988) and have also been shown to correlate with luminosity (Wells *et al.* 1994; Fisher *et al.* 1995). More recently, Benetti *et al.* (2005) used cluster analysis of measurements of the decline rate of SNe Ia $v_{\rm ej}$ to yield a new way of grouping low-z SNe that perhaps illuminates the role of different explosion mechanisms in SNe Ia diversity. Comparisons of SNe Ia ejection velocities from objects at different redshifts have also been made [e.g. Hook *et al.* (2005); Blondin *et al.* (2006); Balland *et al.* (2006)] demonstrating that the range of velocities measured in SNe Ia ejecta are comparable at all redshifts. Folatelli (2004, F04 hereafter) illustrated the utility of equivalent width (EW) measurements on low-z SNe Ia spectra and Garavini *et al.* (2007) extended this work to compare 12 high-z objects to the low-z population. Hachinger, Mazzali, & Benetti (2006) also illustrated correlations between these EW measurements and the velocity-gradient classification scheme from Benetti *et al.* (2005). Branch *et al.* (2006) presents additional evidence for a temperature or explosion mechanism sequence in SNe Ia with comparisons of different low-z objects in EW-space.

These studies all illustrate how quantitative spectroscopic measurements can be used to explore the factors that affect the heterogeneity and homogeneity of SNe Ia. The utility of these parameters for exploring differences in high-z SNe Ia is limited, however, as the majority of these measurements cannot be reproduced in the high-z data. These limitations are due to the reduced signal-to-noise (S/N), redshift effects (which shift the features to redder regions where sky noise is dominant or moves features out of optical detection limits entirely), host galaxy contamination and the smaller number of observations which all characterise high-z data.

The analysis presented here includes rest frame equivalent width and ejection velocity measurements on a large set of SNe Ia spectra observed for the SNLS with methods that are specifically tailored for high-z data. These measurements are similar to the recently published work of Garavini *et al.* (2007) but are utilized on a much larger high-z set and include a different treatment of host galaxy contamination and estimates of the low-z trends. The studied set of SNe were selected from the objects considered ‘confirmed’ SNe Ia by the SNLS [see Howell *et al.* (2005), H05 hereafter] and used in the survey’s cosmological analysis. These high-z results are compared to corresponding measurements on a set of low-z supernovae from the literature. The results of this investigation address the cosmological implications from high-z SNe surveys by determining whether this SNLS-set of distant objects comprises a population that is spectroscopically similar to their low-z counterparts. An overview of the data sets used in this analysis is presented in Sect. 2. The methods for measureing EW and $v_{\rm ej}$ are presented in Sect. 3. The results and a comparison of the two SNe sets are presented in Sect. 4, in Sect. 5 these results are discussed in more detail and the conclusions are presented in Sect. 6.

2. Spectroscopic Data Sets — Overview

A large number of the SNe Ia that were used to provide the latest constraints on w and other cosmological parameters (Astier *et al.* 2006; Spergel *et al.* 2006) are studied in this paper. Specifically, this includes the SNLS objects observed at the Gemini telescopes during the first year of the survey. This set is augmented by Gemini spectra from the entire 2nd year and part of the 3rd year of SNLS observations, which are published here for the first time. This section briefly describes the observation, data reduction, and identification of these SNLS SNe spectra in Sect. 2.1. In Sect. 2.2 a summary of the set of low-z SNe that were quantitatively compared to the distant SNe Ia is provided.

2.1. High Redshift SNLS Supernovae

2.1.1. SNLS Spectra – Observation, Data Reduction and Classification

Full details of the methods used for SNLS SN candidate selection and observation can be found in Sullivan *et al.* (2006) and H05, respectively. In summary, the Canada-France-Hawaii Telescope Legacy Survey (CFHTLS), using the Megacam wide field imager, acquires real time lightcurves of possible SNe by repeatedly imaging four, one square-degree fields approximately every four days (observers’ frame) in several filters (a combination of g’, r’, i’, and z’) as part of the Deep component of the CFHTLS. Spectroscopic observations are then made at 8m-class telescopes in order to identify the SN-type and redshift of these candidates.

The objects studied here were observed at the Gemini North and South telescopes with the Gemini Multi Object Spectrograph [GMOS; (Hook *et al.* 2004)] in longslit mode. Typically, three 20 minute to 30 minute exposures are taken of each candidate. The GMOS R400 grating (400 lines per mm) and 0.75” slit are used, which gives a 6.9 Å spectral resolution. A central wavelength of 680nm was chosen for objects at an estimated $z \lesssim 0.4$ and objects at higher estimated z are observed with a central wavelength setting of 720nm. This central wavelength selection is important in order to ensure that the defining SiII features (located at rest wavelengths of $\sim$ 4100 Å and $\sim$ 6150 Å) of SNe Ia spectra are observed. The 680 nm setting was paired with the GG455_G0305 order-sorting filter to provide wavelength coverage from 4650 Å to 8900 Å. The 720 nm setting was used along with the OG515_G0306 order-sorting filter to cover wavelengths from 5100 Å to 9300 Å. Queue observing was employed to observe the SNLS candidates, which require better than 0.75” image quality (corrected to zenith), in either classical or nod-and-shuffle (N&S) observing modes (see H05).

The reduction of the spectra was completed using IRAF[1], independently from that of H05, but with very similar methods. The independent reductions were made to check for any systematic differences in the pipelines and the results from all reductions were in very close agreement.

---

[1] IRAF is written and supported by the IRAF programming group at the National Optical Astronomy Observatories (NOAO). NOAO is operated by the Association of Universities for Research in Astronomy (AURA), Inc. under cooperative agreement with the National Science Foundation

To classify the SNLS objects, the final spectra are quantitatively compared to template supernovae from large library of low-*z* objects with a χ^2 matching program [see Howell & Wang (2002) and H05 for details]. The results from this matching program and the opinions of SNLS members are used to rank the identifications according to one 'confidence index' (CI) from the six categories defined in H05, with a 5 being a 'Certain Ia' and a 0 as 'Not a Ia'. Objects that are ranked at a CI of 3 or greater are considered 'confirmed' Type Ia SNe. These are the objects that were used in the cosmology fits from Astier *et al.* (2006) and also make up the 80 high-*z* SNe Ia studied here.

The selection criteria of the SNLS sample means that Type Ia SNe at high-*z* with properties that are very different from those seen nearby are likely to be rejected. Thus in the comparisons below the existence of a new population of high-z SNe with unusual properties cannot be ruled out. However as will be seen later, the selection process does allow a range of SNIa properties through, and thus tests for evolution within this range are possible.

2.1.2. Summary of the SNLS Dataset

The SNe candidates observed during the first year of the survey at the Gemini telescopes were published in H05. Table 2 of H05 lists the derived properties of these spectra. This set includes 64 candidates observed from August 2003 through October 2004. Within this set, 41 objects were classified with as confirmed SNe with a CI $\geq$ 3 and are studied here.

Spectra from the entire second year and part of the third year of SNLS observations at Gemini are presented here for the first time. These spectra were observed between November 2004 and May 2006. During this period 59 SNe candidates were observed and 46 of these objects were confirmed as SNe Ia. The setup and conditions of the observations of these objects are listed in Table 6. The derived properties and final classifications of these spectra are summarized in Table 7. Some example spectra are presented in Fig. 1 and all of the spectra are available in the on-line version of this paper.

For the analysis in this paper we make use of not only spectral properties but also photometric properties. The latter are derived from lightcurve fits to the SNLS CFHT photometry, following the methods described in Astier *et al.* (2006). The main lightcurve parameters used are the date of B-band maximum light, and percentage increase relative to the host galaxy (interpolated to the date of spectroscopy).

2.2. Low Redshift Type Ia Supernovae

2.2.1. Low-*z* Spectra

The spectra that make up the low redshift sample in this study were selected from the literature. A majority of these spectra can be found on the online Supernova Spectrum Archive (SUSPECT[2]). The main goal of this study is to quantify the similarities and differences between high-z SNe Ia and those discovered locally, so objects with epoch and wavelength coverage that approximated that of the SNLS sample were selected. These spectra were corrected for peculiar velocities and redshift where appropriate. All of the low-*z* objects that met this criteria are listed in Table 1.

The low-*z* sample includes 167 spectra from 24 different objects. The set includes the so-called 'core normal' (Branch *et al.* 2006) objects [*i.e.* SNe similar to SN 1981B (Branch *et al.* 1983), SN 1989B (Barbon *et al.* 1990; Wells *et al.* 1994), SN 1992A (Kirshner *et al.* 1993) or SN 1994D (Patat *et al.* 1996)] as well as spectroscopically peculiar SNe Ia such as the overluminous 1991T-like objects and underluminous 1991bg-like SNe.

2.2.2. Low-*z* photometry and distance estimation

The photometric properties of these nearby objects are listed in Table 2. These properties have been presented in the literature (Perlmutter *et al.* 1999; Phillips *et al.* 1999; Altavilla *et al.* 2004; Reindl *et al.* 2005) with slightly different results depending on the color corrections used or the lightcurve fits to the published photometry. To remove systematic differences when comparing results, the photometry from these SNe was re-fit by SNLS members to derive the magnitudes and lightcurve shape parameters used later in this analysis. This lightcurve fitting used a new template spectrum for K-corrections [see Hsiao *et al.* (*in press*) and Conley *et al.* (*in prep*) for full details]. The parameters derived from these fits are summarized in Table 2.

These re-derived photometric properties were also used to estimate the absolute peak (B') magnitudes, $M_{\mathrm{B_{peak}}}$, of the low-*z* SNe Ia. A new estimate of these magnitudes is of interest as the published values have [in general, see Phillips *et al.* (1999) and Altavilla *et al.* (2004) for exceptions] already been corrected for a derived lightcurve shape-luminosity correction. In order to fully explore the homogeneity of SNe at different redshifts and to investige any possible spectroscopic sequences in SNe Ia, an uncorrected, or intrinsic, $M_{\mathrm{B_{peak}}}$ is desired.

To make this estimation, the observed magnitudes from Table 2 were first corrected for host galaxy reddening using the relation between $\Delta m_{15}(B)$ (estimated from the re-fit lightcurves) and $B - V$ colour described by Eq. 7 in Phillips *et al.* (1999). Combined with the relations in Eq. 9 and Eq. 11 from the same publications, the observed and estimated 'true' $B - V$ colours were approximated to constrain the host galaxy reddening for each SN. This is the only step of the estimate that made use of a SNe Ia lightcurve shape-luminosity correction and is unavoidable as some assumption of the intrinsic colour of these objects is necessary to infer the host galaxy reddening. This reddening was then converted to a B'-extinction with $R_B = 3.0$. This is not the standard value used in this exercise and does not take into account extremely red objects (Elias-Rosa *et al.* 2006), but it is approximately the median value of the different R_B estimates in the literature. The selection of this R_B value does not have a large effect on the results in this paper. A different R_B would systematically shift all the values in Table 2 a slight amount, but leave the relative relationship between the magnitude of the different SNe the same, which is the true parameter of interest in this study as illustrated in Fig. 10.

Next, the distance modulus, μ, to the host galaxy was used to convert to an absolute magnitude via $\mu = m - M$ (where m and M are the observed and absolute magnitudes, respectively). To yield the most correct distance modulus, the authors used the most reliable Cepheid variable based distances to the SNe host galaxies that were available in the literature. These distances were available for 9 of the SNe in Table 1 and another 5 low-*z* SNe had reliable host distances from the *Nearby Galaxies Catalogue* (Tully 1988). The remaining objects did not have any independent distance constraints and were not considered for these M_B estimates. The errors in each of these steps

---

[2] `http://bruford.nhn.ou.edu/suspect/index1.html`

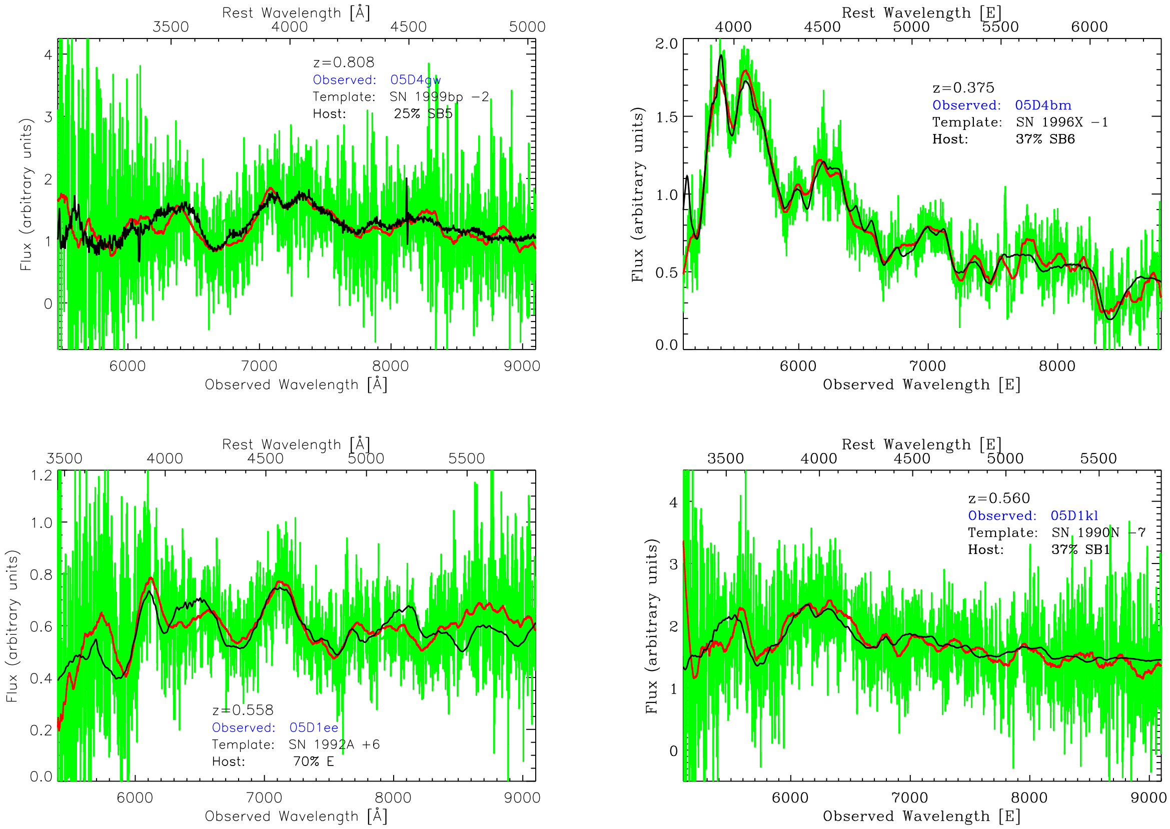

Fig. 1. Example spectra of SNLS candidates observed by Gemini. The observed spectra after subtraction of the best-fitting host galaxy template are displayed in green. The smoothed spectra are shown in red and the best fitting template SNe are overplot in black. The top two objects are ‘certain type Ia’ SNe (CI = 5) as they have clear signs of SiII. The bottom objects are SNLS candidates with CI = 4 (*left*) and CI = 3 (*right*). These spectra match SNe Ia templates but have ambiguous SiII absorption. All of the other spectra are available online.

Table 3. Wavlength regions for the SNeIa features defined by F04.

Feature Number	Label	Blue-ward Limit (Å)	Red-ward Limit (Å)
1	‘CaII H&K’	3500 - 3800	3900 - 4100
2	‘SiII 4000’	3900 - 4000	4000 - 4150
3	‘MgII’	3900 - 4150	4450 - 4700
4	‘FeII’	4500 - 4700	5050 - 5550
5	‘SII W’	5150 - 5300	5500 - 5700
6	‘SiII 5800’	5550 - 5700	5800 - 6000
7	‘SiII 6150’	5800 - 6000	6200 - 6600

were propagated through this estimate to provide a final error on M_B. The final column in Table 2 lists these intrinsic peak magnitude values for the 14 low-z SNe that had reliable, independent distance estimates and secure observed photometric properties.

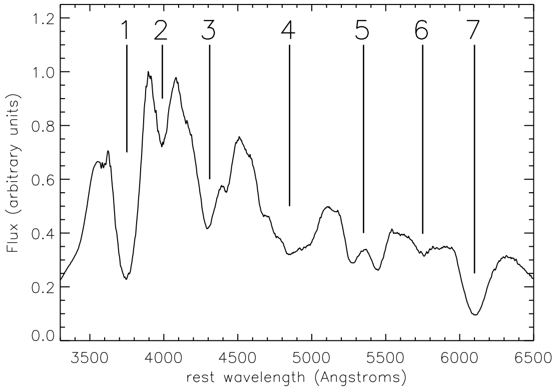

Fig. 2. The spectroscopic regions of specific interest to SNe Ia EW measurements, as defined by F04, are shown here on a core normal SN Ia near maximum light. The wavelength ranges and nomenclature for these features is summarized in Table 3.

3. Spectroscopic Analysis Techniques

3.1. Equivalent Widths

Rest frame equivalent width measurements are a shape-independent method of quantifying the strength of spectroscopic features. The method used in this EW analysis is similar to F04 and Garavini *et al.* (2007), which defined eight regions that contain the strongest absorption features observed in core normal SNe Ia spectra near maximum luminosity. The first seven regions are illustrated in Fig. 2, and the nomenclature and wavelength ranges used to define them are given in Table 3. For supernovae, the continuum needed to make the EW measurement is not well defined, so it is estimated by making a straight line fit between

Table 1. The low redshift spectra analyzed in this study. The dates correspond to the epoch relative to maximum luminosity in the B-band. Many of these spectra are available in the SUSPECT archive as well as their listed publications.

Name	Date(s)	Reference
1981B	0,20	Branch *et al.* 1983
1986G	-5,-4,-3,0	Phillips *et al.* 1987
1989B	-7,-5,-3,-2,-1,3,5,8,9,11,12,13,16,17,18,19	Barbon *et al.* 1990, Wells *et al.* 1994
1990N	-14,-7,2,3,17	Mazzali *et al.* 1993
1991M	3	Gomez & Lopez 1998
1991T	-12,-11,-10,-8,-7,-6,0,10,15	Mazzali, Danziger, & Turatto 1995
1991bg	0,1,2	Turatto *et al.* 1996
1992A	-5,-1,3,5,6,7,9,11,16,17	Kirshner *et al.* 1993
1994D	-11,-10,-9,-8,-7,-5,-4,-2,2,4,10,11,12,13,20	Patat *et al.* 1996
1994Q	10	Gomez & Lopez 1998
1996X	-2,-1,0,1,2,7	Salvo *et al.* 2001
1997br	-9,-8,-7,-6,-4,8	Li *et al.* 1999
1997cn	3	Turatto *et al.* 1998
1998aq	-8,0,1,2,3,4,5,6,7	Branch *et al.* 2003
1998bu	-4,-3,-2,8,9,10,11,12,13	Capellaro *et al.* 2001
1999aa	-11,-3,-1,5,6	Garavini *et al.* 2004
1999ac	-15,-9,0,2,8,11	Garavini *et al.* 2004
1999aw	3,5,5,12	Strolger *et al.* 2002
1999by	-5,-4,-3,-2,3,4,5,6,7,8,11	Garnavich *et al.* 2004
1999ee	-11,-9,-8,-6,-4,-2,-1,0,3,5,7,8,9,12,14	Hamuy *et al.* 2002
2000E	-2,3,5,14	Valentini *et al.* 2003
2000cx	-4,-3,-2,-1,0,1,5,6,7,9,11	Li *et al.* 2001
2002bo	-14,-13,-11,-7,-6,-5,-4,-3,-2,-1,4	Benetti *et al.* 2004
2003du	-11,-7,13	Anupama, Sahu, & Jose 2005

the local maxima that bound each feature. The following rules govern how the continuum is set:

- the pseudo-continuum is always set within the feature regions listed in Table 3
- the feature boundaries are selected to maximise the wavelength span of the measurement without intersecting the boundaries of any neighboring features
- the EW is always calculated in the rest frame

The continuum is set automatically but a human judgement is made on its placement to ensure the guidelines above are followed. The EW is then calculated by numerically integrating underneath this 'pseudo-continuum' at every wavelength pixel λ_i (for all N points within the set continuum bounds):

$$EW = \Sigma_{i=1}^{N}\left(1-\frac{f_\lambda(\lambda_i)}{f_c(\lambda_i)}\right)\Delta\lambda_i \qquad (1)$$

where f_λ is the flux level of the spectrum, and f_c is the flux of the pseudo-continuum. The statistical uncertainty in the EW measurement is calculated by propagating the estimated uncertainties in the flux and pseudo-continuum:

$$\sigma_{EW}^2 = \Sigma_{i=1}^{N}\left(\{\frac{\sigma_f(\lambda_i)}{f_c(\lambda_i)}\}^2+\{\frac{f_\lambda(\lambda_i)}{f_c(\lambda_i)^2}\}^2\cdot\sigma_{c_i}^2\right)\Delta\lambda_i^2 \qquad (2)$$

here σ_f is the measurement uncertainty in the flux and σ_{c_i} is the uncertainty in the pseudo-continuum flux. The σ_{c_i} is calculated via the propagation of the correlated errors in the selection and calculation of this continuum.

In addition to the error calculated in Eq. 2, uncertainties can be caused by variations in the extent or the slope of the pseudo-continuum. The range and effects of these possible pseudo-continuum variations were estimated by randomly shifting the continuum boundaries within $\frac{R}{4}$ Å of the selected maxima (where R is the range of the feature boundaries, see Fig. 2) for the feature and spectrum in question. The EW was then re-measured, and the standard deviation of these measurements (which were repeated 50 times) was accepted as an approximation of this error in each EW measurement. For the high S/N spectra, the possible variations in the continuum were found to be the dominant source of error. The high-z data was subject to some additional systematic errors, so this general procedure had to be amended for these objects; this is discussed in the following section.

In calculating the low-z EW, any possible effects from noise fluctuations were mitigated by setting the continuum end-points to an average flux value that was computed over a 25 Å window around the selected maxima. Observed error spectra were not available for most of the objects in this nearby sample, so the statistical error could not be calculated. However, the dominant error from the possible pseudo-continuum variations was estimated as described above. In total, these uncertainties were on the order of $5-10\%$ of the measured low-z EW. This measurement techniqe differs slightly from previously published EW studies (F04; Hachinger, Mazzali, & Benetti 2006; Branch *et al.* 2006), but the results here are in very good agreement with these other references. Based on the wavelength coverage available in the high-z spectra, this EW analysis is focused on EW features 1, 2, and 3 - CaII H&K, SiII 4000, and MgII in the F04 nomenclature (EW{CaII}, EW{SiII}, & EW{MgII} hereafter).

3.2. High-z EW Measurements

As explained in Sect. 3.2.1, the high-z spectra were median filtered in order to set the feature bounds. The EW measurement was then made with the initial, un-filtered points as Fig. 3 shows.

Table 2. The photometric properties of the low-z spectra analyzed in this study. The published photometry from these objects was re-fit to determine the magnitudes and lightcurve shape parameters shown here. SN 1991M did not have published photometry in B-band, so the parameters for this object were not determined. The SNLS models did not fit the sub-luminous SN 1991bg with any accuracy; the values given here for this unusual object are from Altavilla *et al.* (2004). The precision of the derived values for the unusual SN 2000cx are also in doubt and were not used in any of the analysis in this paper. Uncertainties in each quantity are given in brackets.

Name	z	$\mathrm{MJD}^{a}_{\mathrm{max}}$	m^{b}_{B}	$(B-V)^{c}_{\mathrm{max}}$	s^{d}	$\mathrm{M}^{e}_{\mathrm{B}}$
1981B	0.0060	44671.84(0.09)	11.83(0.01)	-0.06(0.01)	0.95(0.01)	-19.58(0.22)(1)
1986G	0.0027	46560.53(0.05)	11.91(0.01)	0.83(0.01)	0.73(0.01)	· · ·
1989B	0.0024	47564.39(0.27)	12.12(0.02)	0.30(0.02)	0.94(0.01)	-19.03(0.31)(1)
1990N	0.0034	48081.92(0.03)	12.53(0.01)	-0.09(0.01)	1.07(0.01)	-19.59(0.23)(1)
1991M	0.0072	· · ·	· · ·	· · ·	· · ·	· · ·
1991T	0.0060	48374.25(0.04)	11.30(0.01)	-0.04(0.01)	1.05(0.01)	-20.07(0.27)(2)
1991bg	0.0030	48604.50(1.0)	14.75(0.04)	0.00(0.08)	.68(0.10)	· · ·
1992A	0.0063	48639.71(0.02)	12.41(0.01)	-0.09(0.01)	0.85(0.01)	-18.73(0.22)(7)
1994D	0.0015	49431.41(0.01)	11.64(0.01)	-0.19(0.01)	0.84(0.01)	-19.44(0.22)(7)
1994Q	0.0294	49494.35(0.90)	16.16(0.09)	-0.14(0.04	1.11(0.04)	· · ·
1996X	0.0070	50190.65(0.10)	12.86(0.01)	-0.12(0.01)	0.90(0.01)	-19.38(0.22)(7)
1997br	0.0053	50558.57(0.03)	13.23(0.02)	0.12(0.01)	0.89(0.01)	· · ·
1997cn	0.0162	50593.36(0.32)	18.12(0.02)	0.92(0.01)	0.89(0.02)	· · ·
1998aq	0.0037	50930.16(0.02)	12.18(0.01)	-0.25(0.01)	0.98(0.01)	-19.87(0.23)(6)
1998bu	0.0030	50951.89(0.04)	11.97(0.01)	0.15(0.01)	0.99(0.01)	-19.18(0.26)(1)
1999aa	0.0144	51231.82(0.03)	14.59(0.01)	-0.18(0.01)	1.12(0.01)	· · ·
1999ac	0.0095	51250.07(0.08)	13.99(0.01)	-0.08(0.01)	1.02(0.01)	· · ·
1999aw	0.0380	51253.34(0.08)	16.59(0.01)	-0.17(0.01)	1.22(0.01)	· · ·
1999ee	0.0114	51468.89(0.01)	14.69(0.01)	0.11(0.01)	1.05(0.01)	-19.70(0.30)(3)
2000e	0.0047	51576.44(0.03)	12.68 (0.01)	0.01(0.01)	1.03(0.01)	-20.08(0.25)(7)
2000cx	0.0079	51752.03(0.03)	12.92(0.01)	-0.09(0.01)	0.91(0.01)	· · ·
2002bo	0.0042	52356.43(0.04)	13.82(0.01)	0.29(0.01)	0.95(0.01)	-19.04(0.46)(7)
2003du	0.0064	52766.22(0.19)	13.36(0.01)	-0.25(0.01)	1.02(0.01)	-19.53(0.45)(5)

a – date of maximum luminosity (rest-frame B')

b – maximum apparent magnitude in rest-frame B' magnitudes, corrected for Milky Way extinction with E(B-V) values from Schlegel et al. (1998)

c – $B-V$ color at (B-band) maximum luminosity

d – stretch values, based on fitting a fiducial $s = 1.0$ Type Ia template

e — absolute peak luminosities (B'), **not** adjusted for lightcurve shape-luminosity corrections. These made use of the following distance modulus references - 1: Gibson *et al.* (2000) 2: Saha *et al.* (2001) 3: Stritzinger *et al.* (2002) 4: Candia *et al.* (2003) 5: Anupama, Sahu, & Jose (2005) 6: Riess *et al.* (2005) 7: Tully (1988)

For the SNLS data set, the available statistical uncertainty was used to weight each point so that the equivalent width was calculated as

$$EW_{\mathrm{SNLS}} = \left(\Sigma_{i=1}^{N}\left(1 - \frac{f_\lambda(\lambda_i)}{f_c(\lambda_i)}\right)\Delta\lambda_i w_i\right)\frac{N}{\Sigma(w_i)} \tag{3}$$

where w_i is the weighting function at each point:

$$w_i = 1/\sigma_f(\lambda_i)^2 \tag{4}$$

The statistical errors were calculated as defined in Equation 2. The error induced by any variance in the pseudo-continuum was computed with the method described in Sect. 3.1. A description of the errors caused by sky noise and host galaxy contamination is presented in the next sections.

Note that if either the lower or upper range of an EW measurement (defined in Table 3) was outside of the observed wavelength range then the measurement had to be removed from further analysis. This constraint affected results on a measurement-by-measurement basis and caused the removal of 61 EW measurements in the SNLS data set. This left a total of 217 measurements from 73 different high-z SNe in the final set of EW results. A number of these measurements were later removed for host contamination considerations, however (see Sect. 3.2.2).

3.2.1. High-z EW Systematic Errors I – Signal to Noise

The sky noise affects the high-z measurements by augmenting the local maxima selected to set the pseudo-continuum. This can result in an overestimate of the equivalent width. A median filter was used to correct this systematic effect. The size of the filter window was selected via simulations in which spectra from the low-z sample were degraded with noise to match that in the high-z SNe. The EW was then re-calculated on each of the artificial spectra, using a median filter set to various window sizes. Using a median filter over a 60 Å window proved to be the most robust for all measurements at the wide range of S/N levels covered by the high-z spectra.

These simulations were also used to check that the uncertainties in EW measurements behaved as expected for a given signal-to-noise input spectrum. Both the simulations and the final measurement results demonstrated that the statistical errors in the high-z sample were approximately 7% – 20% of the measured EW value. This is nearly twice the uncertainty of the low-z objects due to their reduced S/N.

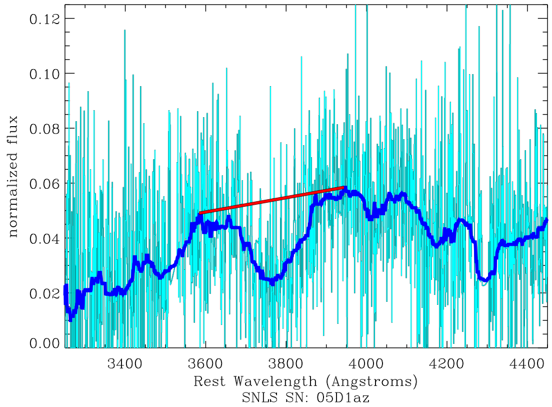

Fig. 3. An example of an EW measurement (for EW{CaII} in this case) on a high-z SNLS object. The median filtered spectrum is plotted on top of the observed spectrum. The local maxima of the feature have been found within this median filter. The EW is then computed by numerically integrating the weighted, un-filtered flux underneath the pseudo-continuum defined by the two maxima.

3.2.2. High-z EW Systematic Errors II – Host Galaxy Contamination

In nearby objects, the angular separation between the host and SN candidate is enough that most observations are not affected by host galaxy light. This is not the case with distant SNe. In previous high redshift spectroscopic studies, this error has been addressed by subtracting host galaxy templates during the χ^2-fitting process (Howell & Wang 2002; Hook *et al.* 2005; Garavini *et al.* 2007), during the extraction of the SN spectrum (Blondin *et al.* 2006), or not at all. In reality, the host contamination tends to 'wash out' the absorption troughs in SNe spectra, which causes the measured strength of these features to be lower than what would be seen in a spectrum free of host galaxy flux. The actual effects of the contamination are dependent on the redshift and host galaxy type of each object in addition to the amount of contamination. The rolling search method of the SNLS provides extensive photometric data that was used to estimate the amount of host galaxy contamination at the epoch of spectroscopy for each SN.

Each object in the SNLS sample has epochs of non-detection before and after the explosion. These are used as a baseline from which to calculate the precentage increase of the SN light over that of the host galaxy on each date when photometry was taken. A 1.10" (diameter) circular aperture centred on the SN is used as it is the basis for the percent contamination estimates that the SNLS photometric pipeline provides for each SN candidate. By interpolating these measurements to the date of spectroscopy, the amount of host contamination in the supernova spectrum can be estimated.

In order to do this, the fact that the spectroscopic aperture is not the same size and shape as the photometric aperture must be taken into account. The spectroscopic aperture is rectangular, with a width of 0.75" and a length set by the extraction window used during the spectroscopic data reduction. The amount of host light entering the slit was simply scaled from that in the 1.10" photometric aperture by assuming a spatially flat profile. The amount of SN light entering the slit was estimated by modelling the SN signal as a two-dimensional PSF with a FWHM equal to the seeing in the appropriate GMOS acquisition image. The photometrically determined percent increase can thus be converted to a 'percent contamination' of host flux in the observed spectrum.

The effects of host contamination on the EW results was determined by artificially contaminating low-z spectra from several different SNe Ia with template galaxy spectra from E, S0, Sa, Sc, and starburst galaxies. In each run of the simulation, the range of the observed CFHT i'-band was shifted, based the redshift of each SNLS object, to where it would fall in the rest frame. The i'-band was chosen because this is the wavelength region where SNe Ia are brightest for the redshift range of this survey; most of the SNLS observations are thus made in this band. The flux of a chosen host galaxy template was then scaled to match the level host contamination (estimated as described above) and added to the low-z supernova spectrum. The EW was re-measured to give the percent error caused by the specific host type and contamination amount for every EW measurement on each SNLS object.

The results of these simulations were then used to correct for this systematic error in the high-z spectra. The median value of the percent error estimates among the different low-z spectra was used as the best estimate for the contamination effects on each SNLS supernova, EW measurement, and galaxy type in question. The uncertainty of this percent error estimate was quantified with the standard deviation of the contamination effects from different host galaxy and SNe templates. The effects within each general host galaxy type were similar, so this uncertainty was only 5% – 7% of the measured EW. Including the excess statistical uncertainty from reduced S/N, this error means that the uncertainties in the high-z EW results are roughly 2-3 times those in the corresponding low-z set. The galaxy type for the SNe was selected based on the observed host features in each affected SNLS spectrum. The results of these corrections on the measured EW values are displayed in Fig. 5.

The results of these simulations helped determine that objects with greater than 65% host contamination were too biased to be included in the final analysis of this data set. This is because at this contamination level, a majority of the high-z EW results require adjustments greater than 100% of the measured EW and this amount of host flux severely alters the shape of the SNe spectra so that the local maxima for each feature cannot be identified in a manner consistent with the rest of the sample. This removed measurements from 19 objects (in addition to the measurements removed for observed-wavelength restrictions). The final set of high-z results thus includes a total 162 EW measurements from 54 SNLS SNe Ia.

3.3. Ejection Velocities

The distribution of the ions in the homologously expanding SN photosphere and the kinetic energy of the thermonuclear explosion are expressed in the ejection velocities measured in the SN spectrum. Measurements of the ejection velocities of the features attributed to CaII H&K, SII (near λ5640) and SiII (near λ6150) — our EW features 1, 5, and 7, respectively — have previously been studied in both nearby (Branch *et al.* 1988; Wells *et al.* 1994; Fisher *et al.* 1995; Mazzali *et al.* 1998; Benetti *et al.* 2005; Mazzali *et al.* 2005) and high redshift (Hook *et al.* 2005; Blondin *et al.* 2006) SNe Ia populations. The redshifts of the distant objects that make up the bulk of the SNLS sample are high enough that the SII 'W' (λ5640) and SiII λ6150 features are generally not observed, so only the CaII H& K feature was studied.

The ejection velocity, $v_{\rm ej}$, was calculated as the blueshift of the minimum of the feature away from an estimated rest wavelength of 3945.0 Å (a weighted average of the two components of the CaII H&K feature). The contribution of other ions to the absorption in the wavelength range of CaII H&K (most notably SiII), as well the intrinsic distribution of CaII across velocity space, can give this feature a ‘kinked’ shape with two possible minima. This shape makes it difficult to determine where the mininum of the feature is located. This difficulty is compounded by the low S/N of the high-z objects. To make a consistent measurement between the two sets, the entire CaII H&K feature was fit with a Gaussian function. The best fit was estimated with robust, non-linear least-squares MPFIT[3] routine in IDL. The fit was weighted to the most dominant minima of the absorption region by making small, initial Gaussian fits to the deepest, bluest, part of the feature. The wavelength range from this initial fit was then expanded iteratively to span the entire absorption trough, and the minimum of the final fit was used to calculate v_{ej} as

$$v_{\mathrm{ej}} = -c \cdot \left(\frac{(\frac{\lambda_m - \lambda_0}{\lambda_0} + 1)^2 - 1}{(\frac{\lambda_m - \lambda_0}{\lambda_0} + 1)^2 + 1} \right) \tag{5}$$

where λ_m is the measured featured minimum, λ_0 is 3945.0 Å and c is the speed of light. The statistical error for this fit was computed by propagating the uncertanties in the final Gaussian parameters into Eq. 5. An additional source of error, caused by uncertainty in the selection of points used to fit the Gaussian curves, was estimated by taking the difference between the calculated velocities from the initial and final fits.

Without having measurement uncertainties available for the low-z spectra, the statistical errors were not calculated for these objects. For the high-z data, the lower S/N meant these spectra had to be smoothed before the Gaussian fits to the CaII H&K feature could be made. Again a 60 Å median filter was used. The filtered flux was fit with a Gaussian model that was weighted by the error spectra. The statistical error in the final v_{ej} values was estimated by propagating the estimated redshift uncertainties through the velocity calculation.

No corrections were necessary to account for the systematic error from host galaxy contamination as this error was minimal for v_{ej} measurements made on the SNe within the 65% contamination limit discussed in Sect. 3.2.2.

4. Spectroscopic Analysis Results

4.1. Low-z Results

The results of the low-z EW measurements, plotted against rest-frame epoch (relative to B’ maximum light) are shown in the first 3 panels in Fig. 4. The mean trend (and 1σ deviation) exhibited by normal SNe Ia for each feature is shown in the grey contour in each panel. This trend was derived by making EW measurements on a template core normal Type Ia SN spectrum made from a combination of core normal spectra by Nugent, Kim, & Perlmutter (2002). The mean trends for the 1991T-like and 1991bg-like objects were derived from similarly constructed template Type Ia spectra (Nugent, Kim, & Perlmutter (2002); Stern *et al.* (2004); Levan *et al.* (2005), Nugent private communication) and are shown where appropriate. The 1σ deviation shown on these trends was estimated by expanding the error bars on each trend until a fit to the appropriate low-z SNe measurements produced a reduced χ^2 of 1.0. This was done as other methods of estimating the 1σ range would be more dependent on the varying epoch and object sampling of the low-z data set. A constant scatter as a function of epoch was thus assumed, hence the lack of variance over epoch in Figs. 4 - 6.

The core normal objects exhibit fairly homogenous behavior in these EW plots. Not surprisingly, this parameter space also clearly differentiates between the SNe Ia sub-types. The lack of absorption from IME (intermediate mass elements) in 1991T-like objects (which is due to inferred higher temperatures during thermonuclear runaway in these objects) is clearly seen in the EW{CaII H&K} and EW{SiII} results. Similarly, the additional absorption from (primarily) TiII in cooler, 1991bg-like objects results in a significant difference with regards to EW{MgII} measurements. These results are in agreement with the qualitative and quantitative differences that have already been established for these different SNe sub-types (Filippenko *et al.* 1992a,b; Benetti *et al.* 2005; Branch *et al.* 2006).

The changes of CaII H&K v_{ej} with rest-frame epoch is shown in the fourth panel of Fig. 4. The mean trend was estimated by fitting a power law to all of the data points from core normal objects. The core normal objects display a broad trend about this best fit and the SN sub-types are generally interspersed around it. Previous estimations of SN Ia ejection velocities implied that over-luminous objects have significantly higher velocities (Jeffrey *et al.* 1992), but the statistical analysis of SiII velocities by Benetti *et al.* (2005) suggests that these objects perhaps differ in their velocity gradients, which were not studied here as corresponding measurements are not available on the high-z set.

4.2. High-z Results and Comparison to Low-z SNe

The EW measurements on the high-z data before and after correction for host galaxy contamination are shown in Fig. 5. The corrected results are compared to the corresponding low-z results in Fig. 6 and all of these high-z results are listed in Table A in the Appendix.

Figure 6 shows that the general trends exhibited by the low-z sample are indeed followed by the high redshift objects and all of the SNLS results are within the range of the low-z SNe measurements. A few spectra (marked with open circles in Fig. 6) had EW results and other characteristics that are more similar to the SN 1991T-like outliers; these objects are discussed in more detail in Sect. 4.3.

The fraternity between the high redshift SNe measurements and the trends exhibited by the local, core normal objects was further investigated with χ^2 tests. This test compared the high-z measurements to the core normal low redshift ‘model’ illustrated for each feature in Figs. 4 - 6. When making these χ^2 calculations, the full uncertainties for each measurement were used. The 1σ dispersion in the low-z trends was also considered by adding this error (in quadrature) to the uncertainty of each high-z measurement. The uncertainty in the estimated epoch for every high-z result was also added (again, in quadrature) according to the low-z trend for each measurement. The results, shown in Table 4, indicate that there are no statistically significant differences between the spectroscopic features of these SNe Ia for three of the parameters studied here.

The exception to this result is the comparison of EW{MgII} measurements; however, the reality of this difference is questionable. It is possible that this difference is a statistical artifact caused by the differences in the epoch sampling and total number of objects between the high-z and low-z data sets. Figure 4 shows that there are an appreciable number of low-z core normal points between 0 and +10 days past maximum (where the bulk of the outliers in the SNLS set are located) which define the 1σ

---

[3] see `http://cow.physics.wisc.edu/~craigm/idl/`

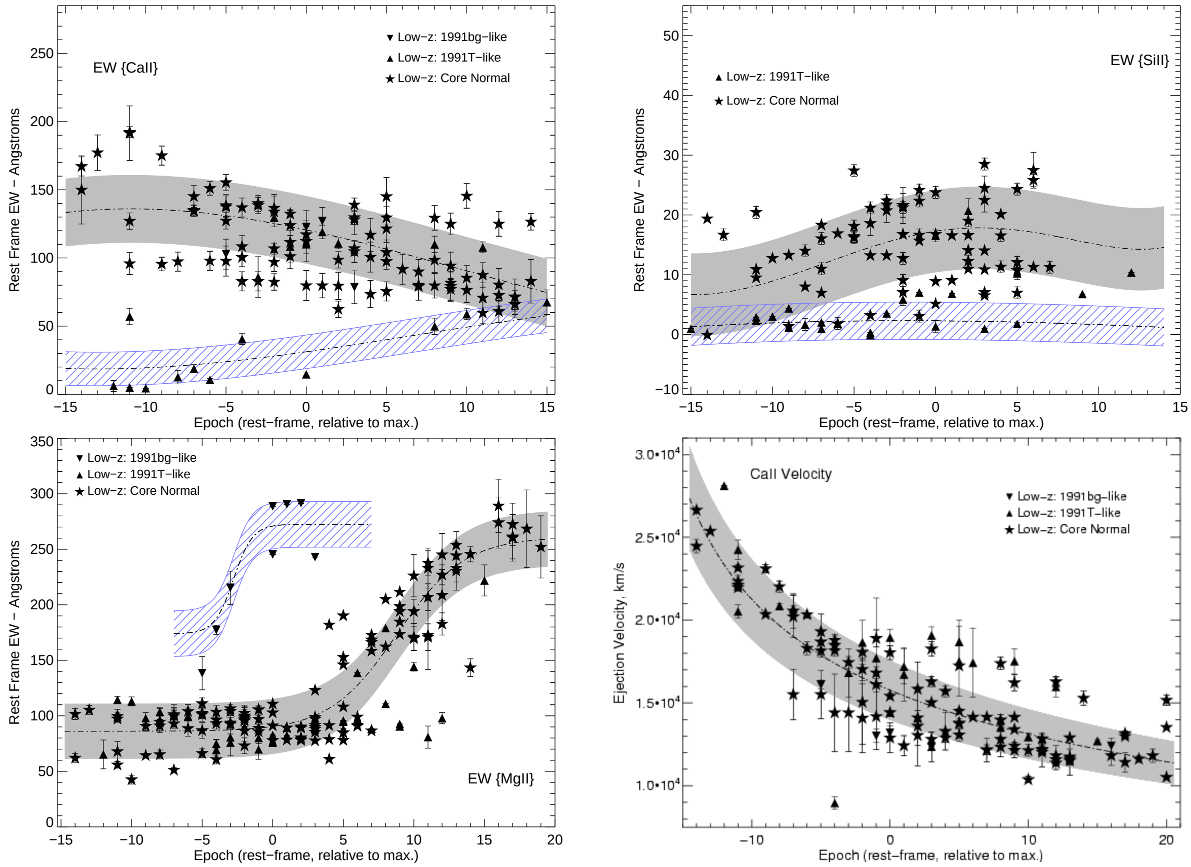

Fig. 4. EW Measurements for the 'CaII H&K' (top, left), 'SiII' (top, right), and 'MgII' (bottom, left) features and CaII H&K v_{ej} (bottom, right) plotted versus rest-frame epoch, for the low-*z* sample. The shaded, grey region marks the mean trend and 1σ distribution of the epoch evolution of these measurements in core normal objects. The striped region marks the same trend for 1991T-like objects in the EW{CaII} and EW{SiII} plots and the trend for 1991bg-like objects in the EW{MgII} plot. These trends were estimated with EW measurements on template SNe Ia spectra from the literature.

Table 4. A quantitative comparison of the spectroscopic features in high-*z* supernovae (as measured with EW and CaII H&K ejection velocities) and the mean trends exhibited for these quantities by local SNe Ia. These results show that there are no significant differences between distant SNLS objects and nearby SNe, with the exception of EW{MgII}.

Feature	Reduced[a] χ^2	DOF[b]	Prob[c]
EW{CaII}	1.10	30	0.67
EW{SiII}	0.47	40	< 0.002
EW{MgII}	1.86	44	>0.999
v_{ej}	1.03	45	0.64

a — χ^2/dof calculated for the measurement/data set in question and the corresponding low-*z* mean trend

b — degrees of freedom used when calculating the reduced χ^2, $N_{\mathrm{datapoints}} - 1$

c — probability (0.00 - 1.00) that the null hypothesis, that the high-*z* data are consistent with the trend displayed by low-*z* SNe, can be rejected.

range on the empirically derived mean trend. Yet these points are from 15 different SNe only; half of the number of SNLS objects in the same range. This sampling difference, combined with the fact that the low-z sample is not well defined (i.e. it is not a complete sample) could mean that the true amount of variance in this feature is underestimated in the low-*z* mean trends, which would artificially increase the significance of the measured difference in the high-*z* results. If this epoch selection effect is not responsible for the difference then it is interesting to consider possible physical interpretations, which we discuss in Sect. 5.

4.3. High-*z* Results: Identification of SNe Ia Sub-Types

The comparisons in Fig. 6 show that a handful of the high-*z* SNLS SNe Ia exhibit spectroscopic features that are more consistent with the 1991T or 1991bg-like SNe from the low-*z* surveys.

Overluminous 1991T-like SNe Ia have less absorption from IME at certain epochs. Three outliers in the EW{CaII} and EW{SiII} results have evidence of being similar to the known class of 1991T-like objects. Their spectra are shown in Fig. 7. 03D4cj displayed a smaller amount of SiII than a typical core normal object. The error bars on this measurement are relatively large (EW{SiII}= 5.9 ± 6.1 Å), but the photometric data for this object supports the conclusion that it is a 1991T-like SN; Astier *et al.* (2006) stated that the lightcurve from this SN was incompatible with the model used to fit all of the other SNLS SNe. The χ^2 template fits to 03D4cj also indicate that it is similar to SN 1991T.

The 1991T-like classification also appears valid for SNLS supernova 03D1cm. This SN has a very low EW{CaII} measurement and an EW{SiII} result that (within large error bars,

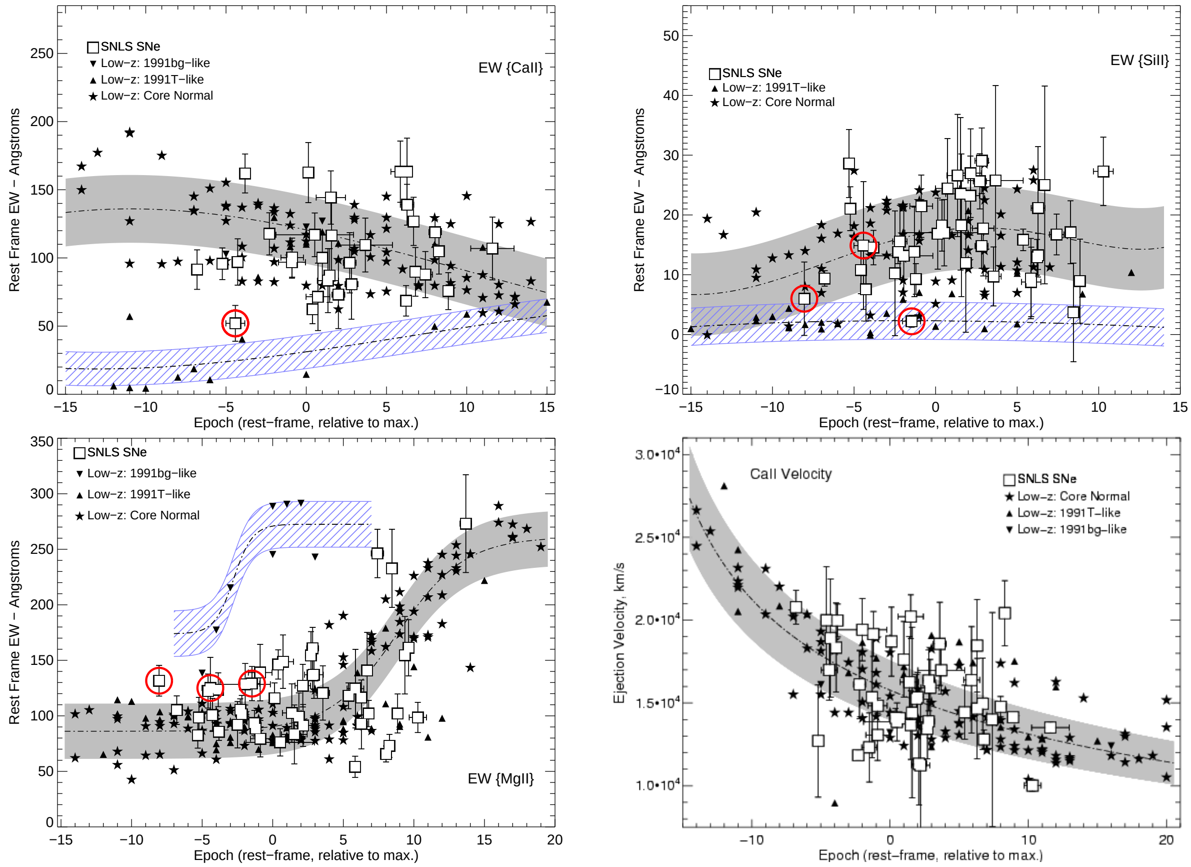

Fig. 6. The results from the SNLS high-z SNe (open squares) compared to the EW results from the low-z sample (filled symbols). The contours in each plot are the same as Fig. 4. The objects that were identified as 1991T-like SNe are circled in red.

EW{SiII} = 14.8 ± 10.6 Å) is also consistent with the low values measured in 1991T-like objects. Photometrically, 03D1cm is also more like a 1991T-like SN as it had one of the highest stretch values from the entire set of Gemini SNLS data at $s = 1.173 \pm 0.061$ (Astier *et al.* 2006). The best matching template spectrum also corresponds to an overluminous low-z SNe. The spectral and photometric dates do differ (+1 day and -4.42 days, respectively) in this case, but the low S/N on this object and inherent uncertainty on spectral dating with this template matching method (which is on the order of a few days) means that this is not necessarily enough evidence to outweigh the 1991T-like EW and s values of 03D1cm.

The SNLS SN 04D3mk also had a very low, well constrained EW{SiII} value. At the epoch this object was observed, the EW{MgII} result cannot differentiate between normal and overluminous SNe and the EW{CaII} measurement was unusable as it fell on the gap between GMOS detectors (e.g., Sect. 3.2). The final photometry of this object did not reveal any photometric peculiarities, but the χ^2 template matches to 04D3mk singled out overluminous SNe Ia spectra only as the most similar low-z objects. This supports the quantitative similarities of 04D3mk to this particular SN Ia sub-type. With this evidence, SNLS objects 03D1cm and 04D3mk are the most distant supernova (at $z = 0.87$ and $z = 0.812$, respectively) to be shown to be spectroscopically similar to the 1991T-like SNe Ia sub-types. To reiterate, the primary source of this identification for these objects is the EW measurements which are quantitatively more similar to the overluminous sub-class of SNe Ia than other sub-types.

The SNLS SNe 03D1co and 05D3mq are 1991bg-like candidates as their large EW{MgII} values are more consistent with the excess absorption measured in the subluminous low-z SNe. However, these two high-z SNe had measurable amounts of SiII, a feature that has yet to be observed in any 1991bg-like SNe because it is obscured by additional absorption from TiII and FeII. This evidence, combined with the normal photometric parameters (Astier *et al.* 2006) derived for these objects and the fact that template matches to 1991bg-like objects resulted in poor χ^2 results, is enough to justify that these SNe are more like core normal SNe than any of the underluminous SNe observed to date.

4.4. Correlations With Host Galaxy Type

4.4.1. Low-z spectra

The general trend of brighter SNe and a higher dispersion of SNe Ia peak magnitudes in late-type galaxies is well documented (Hamuy *et al.* 1996, 2000; Sullivan *et al.* 2003). Yet only a few quantitative spectroscopic corollaries (Branch & van den Bergh 1993; Branch, Romanishin, & Baron 1996) have been made that agree or disagree with this trend. Kolmogorov-Smirnov (KS) tests were thus used to explore any differences between the spectroscopic parameters measured in SNe from different host types in our low-z sample. This test was carried out on the residuals of these measurements, where the residual for each EW and $v_{\rm ej}$ value is defined as the difference between the measurement and the corresponding low-z mean trend.

The host type for each low-z SN was grouped into the broad categories of 'E/S0' and 'Spiral' (Sa, Sb, Sc and irregular) galaxies. The published morphology (from the Nearby Galaxy Catalogue and other appropriate databases) of each SN host

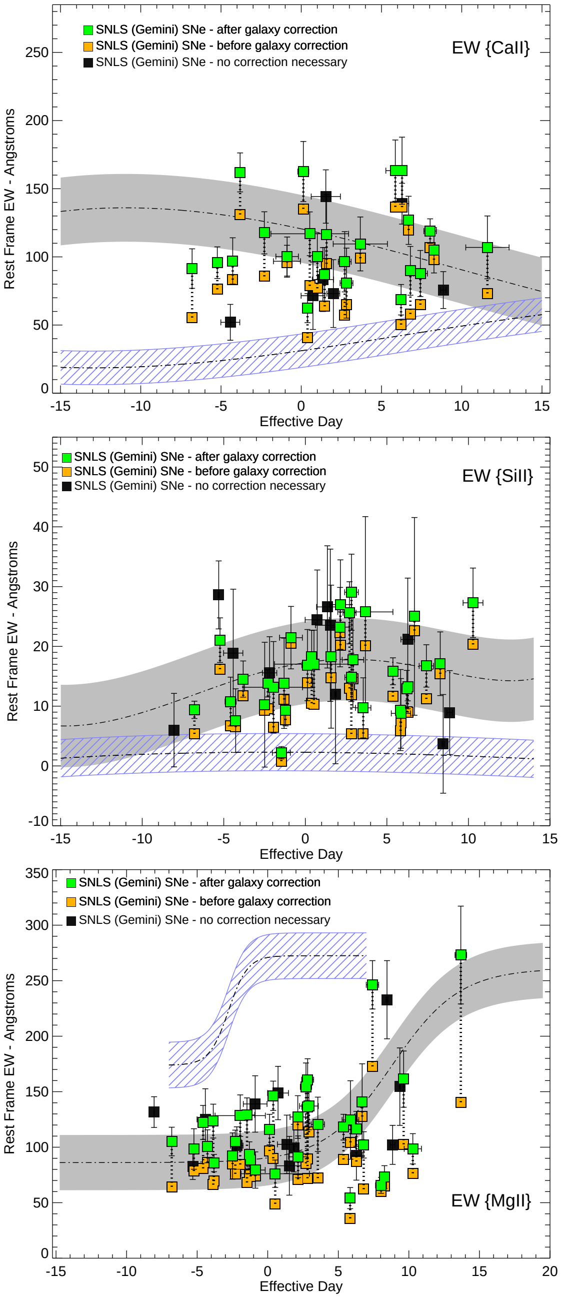

Fig. 5. Measurements of the EW of the ‘CaII H&K’, ‘SiII’, and ‘MgII’ features (from top to bottom), versus rest-frame epoch, in the SNLS high-z sample. The shaded and striped regions are the same as in Fig. 4. The EW measurements that did not need any correction for the systematic effects of host galaxy contamination are shown with the dark, filled squares. All of the other points illustrate the measurements that were corrected for host contamination. The adjusted EW values are connected to the corresponding initial measurements with dotted lines.

galaxy (based on the hosts listed in the SNe reference papers, see Table 1) was used to determine which group was appropriate for each SN host.

A comparison of the residuals for the four measurements discussed in this paper, grouped according to these two broad host galaxy groups, are displayed in Fig. 8. At low-z the only feature that shows a significant trend with host type is SiII.

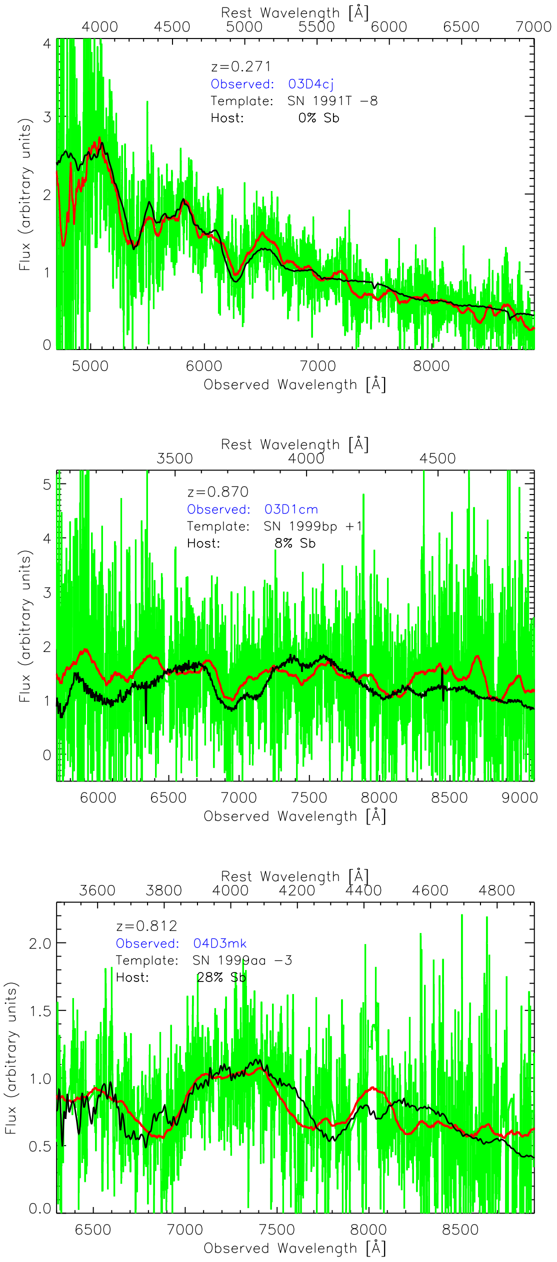

Fig. 7. Three high-z SNe Ia - 03D4cj, 03D1cm and 04D3mk - that demonstrate a quantitative similarity to the 1991T-like SNe Ia sub-type. The green spectrum is the observed spectrum without any binning. The black spectrum is the best-fitting SN from the low-z library and the red spectrum a smoothed version of the observed spectrum. The primary evidence for the similarity of these objects to 1991T-like SNe is the EW{CaII} and EW{SiII} measurements, although in each case the χ^2 fits to SN 1991T or SN 1999aa were quantitatively better than those of core normal SNe Ia. Photometric information also supports this sub-type identification for these three SNe.

4.4.2. High-z spectra

Another test for possible evolution is to determine whether the correlations between low-z SNe Ia characteristics and host morphology are observed within the high-z set. The host types were estimated for the SNLS objects that had clear host galaxy features in their spectra and placed into one of three broad cate-

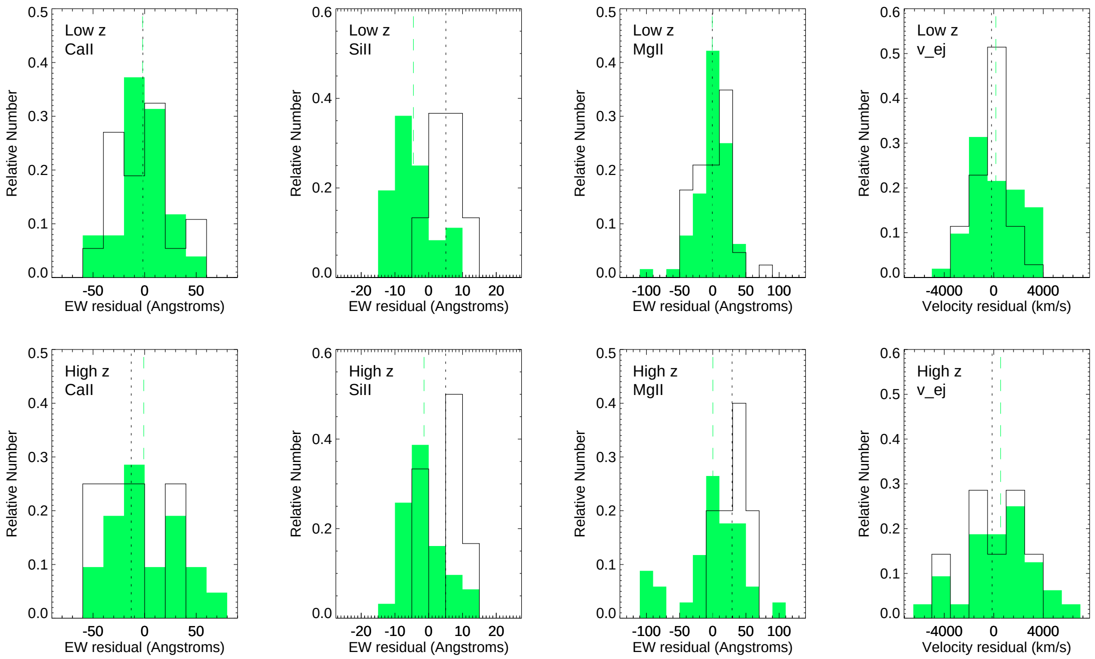

Fig. 8. Histograms comparing the residuals of EW and CaII v_{ej} measurements in SNe from E/S0 (open histograms) and spiral (filled histograms) host galaxies. The residuals from low-*z* SNe are displayed in the top row and the SNLS high-*z* results are on the bottom. The vertical dashed line in each panel is the mean value for each distribution. The histograms have been normalized to have the same area. The distribution of low-*z* SNe results show a significant difference for the objects from early and late hosts (as determined with KS tests). The high-*z* EW{SiII} results show a similar trend while EW{MgII} distributions display a difference that is not seen at low-*z*.

Table 5. Comparison of SNe Ia spectral features in different host types at low and high-*z*. The values given are the mean and error in the mean of the residuals from the low-*z* trend.

Feature	SNe Measurement (low-z trend subtracted)	
	E/S0	Spiral
Low-z		
EW{CaII} - Å	−1.7 ± 4.7	−2.0 ± 3.2
EW{SiII} - Å	5.1 ± 0.7	−4.5 ± 0.9
EW{MgII} - Å	−0.6 ± 3.8	−0.7 ± 2.9
v_{ej} - 1000 km/s	−0.18 ± 0.23	0.17 ± 0.27
High-z		
EW{CaII} - Å	−13.0 ± 16.0	−0.8 ± 7.2
EW{SiII} - Å	5.0 ± 2.4	−1.4 ± 1.1
EW{MgII} - Å	29.1 ± 9.5	0.1 ± 7.7
v_{ej} - 1000 km/s	−0.13 ± 0.90	0.55 ± 0.50

gories; 'E/S0' for early (elliptical and S0 hosts), 'Early Spirals' for objects with spectroscopic features similar to Sa and Sb galaxies, and 'Late Spirals' for Sc and irregular hosts. The subset of SNLS SNe Ia with indentifyable host galaxies includes 45 of the 54 SNLS objects that had EW or v_{ej} results.

The distribution of these SNLS measurements, displayed in the histograms in the bottom of Fig. 8, do show clear similarities to the low-*z* distributions (top, Fig. 8). The distant late type galaxies host SNe that display a smaller amount of SiII than objects from early hosts and the ejection velocities measured in spiral galaxies peak at a higher value. A comparison of the mean values for each measurement (again after subtracting the low-z trend to remove dependence on SN phase) divided by host type supports this conclusion, as can be seen from Table 5.

Similar to the low-*z* results, the high-*z* data show a trend with regards to host type and EW{SiII}, though at a slightly lower significance because of the larger high-*z* uncertainties. We also see a possible difference in MgII that is not seen at low-*z*. Thus, the KS tests of the distribution of high-*z* EW{SiII} and v_{ej} results do not show as significant of a statistical difference between SNe from different host types. This is probably due to the smaller number of measurements in the high-*z* data in addition to the larger errors. For example, the measured maximum deviation between the EW{SiII} distribution in the high-*z* galaxies (KS statistic D) is $D = 0.50$. This value is comparable to the low-*z* $D = 0.64$ and would indicate a significant difference if the high-*z* sample was larger by only 10 measurements.

The trend for lower EWs and higher ejection velocities in late type galaxies seen at low and now also high-z is a corrolary to the broad-band photometric study of SNLS SNe host galaxies completed by Sullivan *et al.* (2006), which showed that the lightcurve shapes of high-*z* SNe demonstrate a dependence on host galaxy star formation rates in a manner consistent with low-*z* objects.

4.4.3. Dependence on Redshift

The high-z EW and v_{ej} measurements (after subtracting the low-z trend to remove the dependence on SN phase) are plotted against redshift in the left-hand column in Fig. 9. No dependence on redshift is seen. Calculations of Spearman's ρ rank correlation and Kolmogorov-Smirnov tests attest that there are no trends in the data with redshift that are significantly different from random scatter. Thus we see no evidence in our sample for systematic evolution of SNe Ia properties in the large redshift range covered by the SNLS.

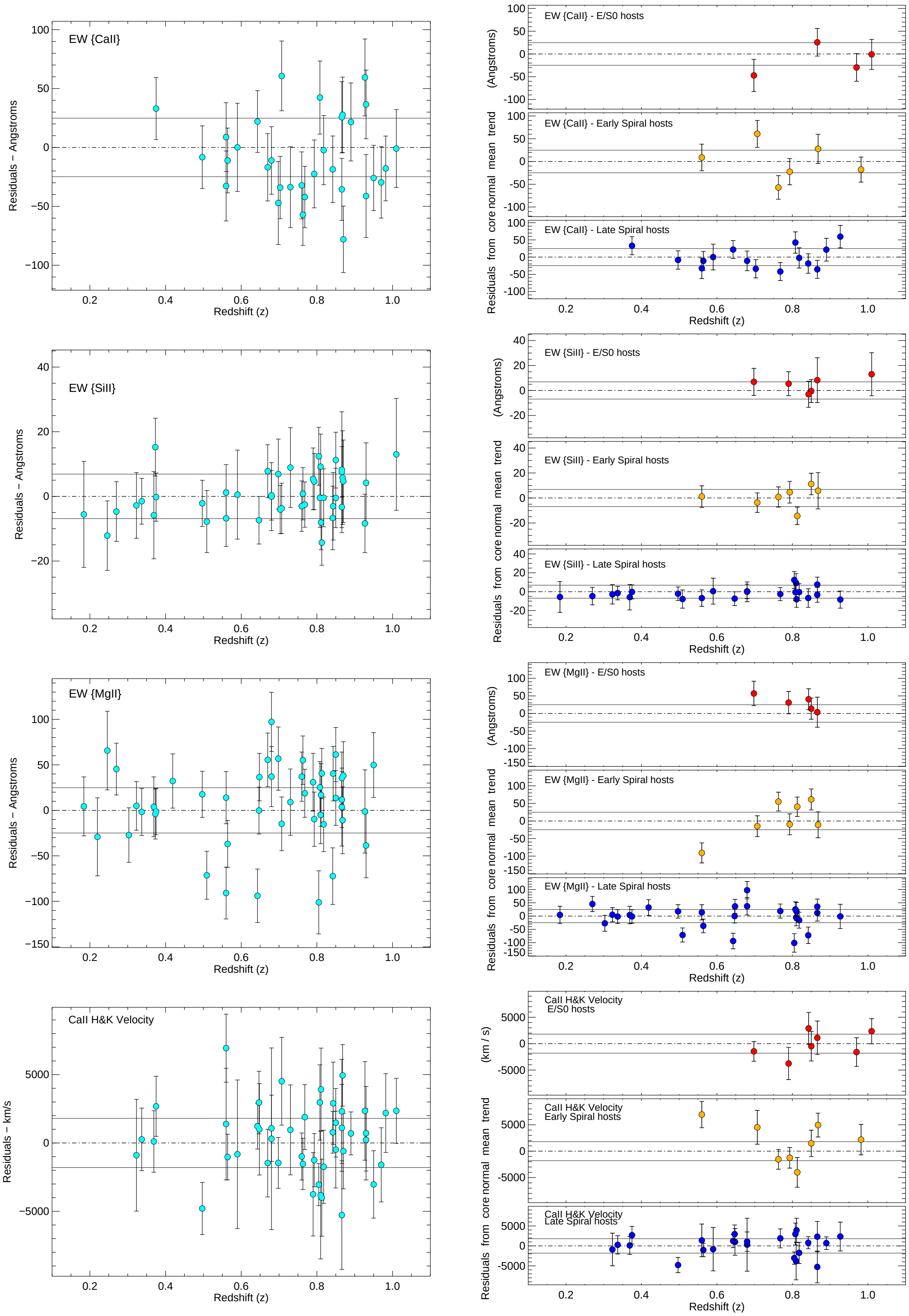

Fig. 9. Left: The high-z residuals (*i.e.* the difference from low-z SNe Ia core normal mean trend) from the EW and $v_{\rm ej}$ measurements are plotted against redshift. Right: the same data divided by host galaxy type.

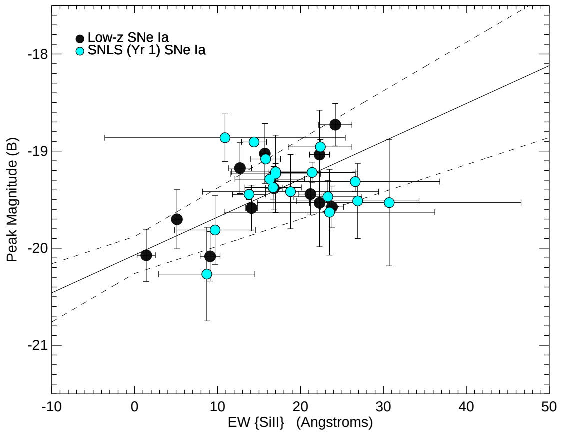

Fig. 10. A comparison of the EW measurement of the 'SiII 4000' feature to the absolute B' peak magnitudes of low-*z* SNe Ia (black circles) and distant SNe (lighter circles). The significant correlation in the low-z data reveals a new spectroscopic sequence in SNe Ia that can be used to estimate SNe Ia peak magnitudes. The high-*z* points have larger error bars with regards to both EW and magnitude, but are still consistent with the low-*z* trend (illustrated with the solid line).

On the right side of Fig. 9, the measurements are divided by host galaxy type. The evolutionary histories of host galaxies within a given morphological category have more in common than galaxies of different classfications. The comparison of SNe Ia spectroscopic features at different redshifts but within similar host types should thus be more sensitive to any evolutionary effects than tests using the bulk properties of the high-*z* sample as a whole. The panels to the right in Fig. 9 illustrate that there are no redshift-dependent trends within the SNe results from each host type.

4.5. EW{SiII} - A New SNe Ia Spectroscopic Sequence

During the course of this study, an interesting correlation was found between EW{SiII} measurements and M_B for the low-z SNe. Figure 10 shows the low-z SNe EW{SiII} measurements, taken as close as possible to maximum light (within ±7.0 days), compared to the absolute peak (B') magnitudes (uncorrected for any lightcurve shape-luminosity relationship) that were estimated for 13 of the low-*z* SNe (see Sect. 2.2.2). A Spearman rank correlation test found a correlation with 3σ significance between the measured EW{SiII} and calculated peak magnitude, M_B. The best fit linear correlation of these quantities is described by the following:

$$M_B = (-20.07 \pm 0.19) + (0.039 \pm 0.011) \times (\mathrm{EW\{SiII\}}). \quad (6)$$

The small residuals from this fit place this spectral indicator on par with others in the literature (Wells *et al.* 1994; Bongard *et al.* 2006; Nugent *et al.* 1995a; Hachinger, Mazzali, & Benetti 2006). This spectroscopic sequence is also relatively free of the epoch constraints on similar sequences (Nugent *et al.* 1995a; Benetti *et al.* 2005; F04) because EW{SiII} evolves little near maximum light and only one measurement is needed to constrain M_B with this correlation. Any single EW measurement near this date (the authors found that ±7.0 days was best as the EW{SiII} values evolved little over this period) yielded the similar results. The wavelength of this feature also makes it ideal as it falls within the optical spectrum out to redshifts of about 1.2 [unlike measurements in the redder end of the spectrum such as the λ5972 feature studied in Hachinger, Mazzali, & Benetti (2006)].

One major physical parameter that underlies this sequence is temperature (Nugent *et al.* 1995a; Branch *et al.* 2006; Baron *et al.* 2006). For an assumed Chandrasekhar mass (M_{CH}) WD explosion scenario, the distribution of peak magnitudes is based primarily on the different amounts of ^{56}Ni synthesised. Higher production of this isotope, which is made at the expense of IME such as SiII, results in a brighter SNe and causes the ejecta to be hotter. This tends to overionise the already smaller amount of IME observed at maximum light thus results in the appearance of a smaller amount of SiII in the spectra of hotter and brighter SNe at these epochs.

Evidence that this spectroscopic sequence is similar at high-*z* is illustrated in the SNLS points in Fig. 10. In this Fig. the absolute magnitudes of the SNLS high-*z* SNe, uncorrected for lightcurve stretch or colour adjustments, were computed assuming the best fit cosmology and published m_B values from Astier *et al.* (2006).

Within the relatively large EW error bars, the SNLS supernovae are still consistent with the low-*z* trends in this parameter space. The next logical step is to determine whether the application of this relation to high-*z* SNe, just like the use of *s* or $\Delta_{m_{15}}$ parameters, decreases the scatter of luminosity distances in a Hubble diagram. This test is displayed in Fig. 11.

For this test, the set of SNLS SNe that were published in the first year SNLS cosmology results and had measured EW{SiII} values were used. A total of 18 SNe Ia from Astier *et al.* (2006) met these criteria. The high-*z* EW{SiII} measurements were used with the relation estimated from the low-*z* sample (Eq. 6) to estimate the absolute peak B-band magnitudes (now termed M_{SiII}).

The distance modulus (μ) for these distant objects was then calculated as

$$\mu = m_B - M_{\mathrm{SiII}}, \quad (7)$$

where m_B is the observed peak B' magnitude previously published in Table 9 of Astier *et al.* (2006). The uncertainties in the linear M_B-EW{SiII} fit and m_B were propagated along with the EW errors during this calculation.

Figure 11 indicates that the EW{SiII} sequence does provide a plausible method to use for estimating peak SNe Ia distances for cosmology. The dispersion in the EW{SiII}-estimated distances about the best-fit cosmological model from Astier *et al.* (2006) is 0.26 mag., which is near the computed residuals of 0.23 mag. from the Astier *et al.* (2006) stretch and colour-corrected SNLS SNe. Both of these values are much improved over the 0.37 magnitude dispersion from the un-corrected SNe magnitudes in this sub-set of 18 high-*z* SNLS SNe. The application of this correlation to SNe Ia cosmology is further discussed in Bronder (2006).

5. Discussion

As discussed in Sec. 4, the spectroscopic measurements and comparisons completed on this new set of distant SNe have shown that these SNLS-observed objects display an overall similarity with the SNe Ia observed at low redshifts. We find no significant difference between the SNe Ia samples for three of the four features studied and a possible difference in the fourth feature (EW{MgII}). We also find similar trends with host type at low and high redshift. Below we discuss these results in the context of the population of progenitors in addition to the rates of various Type Ia sub-types in the SNLS high-*z* sample.

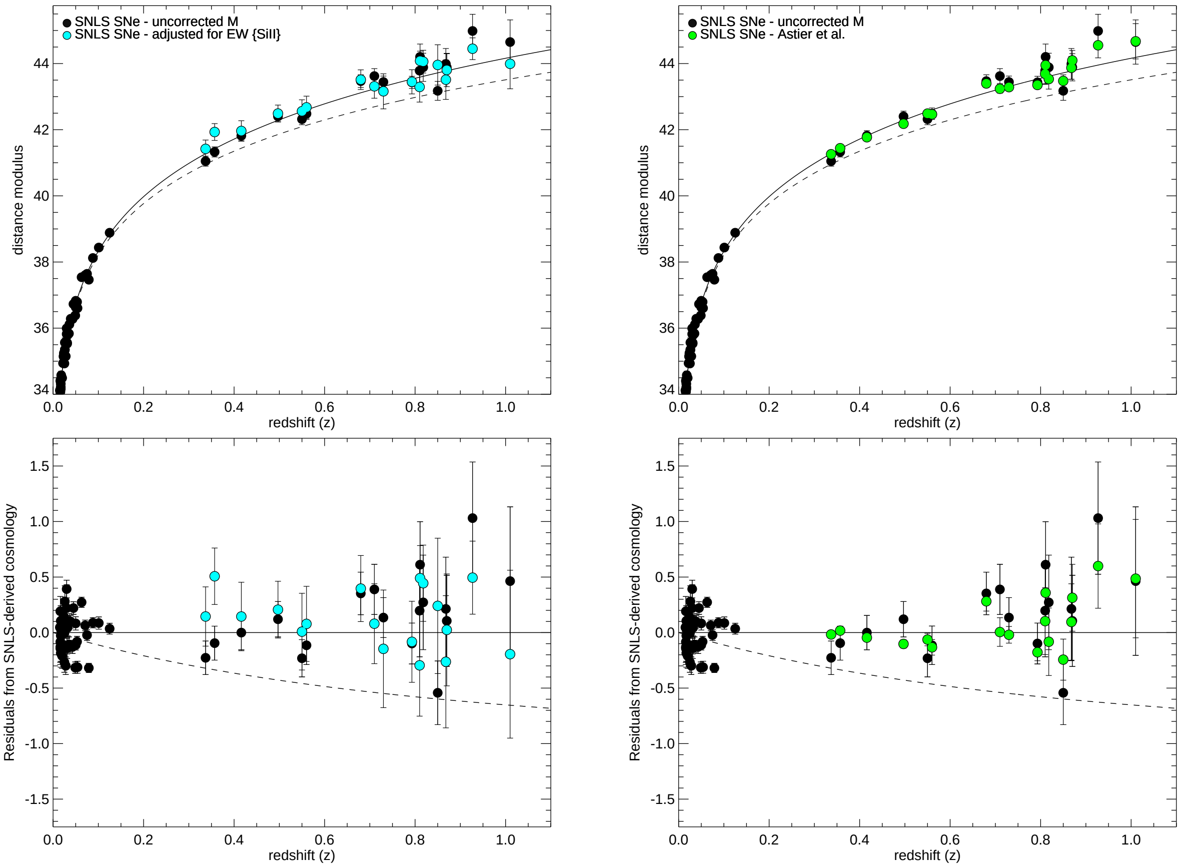

Fig. 11. Hubble diagrams for a subset of SNe Ia from the SNLS first year dataset. Solid points show the distance moduli uncorrected for stretch or colour effects. Left: The lighter (or coloured) points show distance moduli that were calculated with peak magnitudes estimated by the EW{SiII} sequence. Right: The lighter (or coloured) points show distance moduli that were corrected with *s* (stretch) and *c* (colour) corrections (Astier *et al.* 2006). The solid line indicates the best fit cosmology from the first year SNLS results - a spatially flat Universe with $\Omega_M = 0.263$ and $\Omega_\Lambda = 0.737$. The dashed line is the model from a flat Universe with $\Omega_M = 1.00$. The residuals about this cosmology are shown in the bottom two panels; the uncorrected high-*z* SNe points have a dispersion about this cosmology of 0.37 magnitudes, while the EW{SiII} points have a dispersion of 0.26 magnitudes; this is comparable to the 0.23 magnitude dispersion in the Astier *et al.* (2006) results.

5.1. Low-z and High-z Discrepancy - EW{MgII}

In Sect. 4.2 a possible difference in EW{MgII} between low and high-z samples was presented. For the reason given in that section (namely the differences in the time-sampling of observations in the two samples), the significance of this difference may not be high. This was also sugested in a similar study by Garavini *et al.* (2007), who also noted the need for an analysis of a larger sample of normal SNe Ia to more accurately determine the true mean trend for this measurement.

However, it is interesting to consider possible physical explanations, for example it is possible that it is a sign of metallicity differences. Explosion and nucleosynthesis calculations from Travaglio, Hillebrandt, & Reinecke (2005) and Roepke *et al.* (2006), which were computed by modelling thermonuclear burning by deflagration (as opposed to delayed detonation or detonation only) of a C+O WD progenitor, showed that Type Ia SNe from higher metallicity (Z) environments produce a significantly lower (by a factor of 10) amount of ^{24}Mg. In their results, the abundances of Si and Ca were relatively unaffected by metallicity changes. Thus, it may be that the group of high-*z* SNe that are below the mean trend for this feature are all SNe from higher metallicity progenitors. The normal EW{SiII} and EW{CaII} measurements in these SNe support this explanation within the context of these models.

Conversely, model SNe Ia spectra from progenitors of varying Z calculated by Lentz *et al.* (2000) showed the opposite effect in the EW{MgII} measurements. The Lentz *et al.* (2000) spectra were calculated with a similar deflagration model SN [W7 from Nomoto, Thielemann, & Yokoi (1984)], with the metallicity changes approximated by scaling the number abundances of elements heavier than O in the unburned C+O layer. The final IME abundances were not published in Lentz *et al.* (2000), so they could not be compared directly to the Travaglio, Hillebrandt, & Reinecke (2005) results. Instead, the EW measurements defined for this study were made directly on the final Lentz *et al.* (2000) model spectra. These measurements showed that the SNe with higher Z had larger EW{MgII} measurements at pre-maximum epochs but then evolved such that the different Z models were nearly indistinguishable after maximum light.

Another factor that may be contributing to this difference is the trend for the SNLS to find more slightly bluer, brighter objects (Astier *et al.* 2006). F04 noted that the evolution of different SNe along the mean trend for EW{MgII} correlated with luminosity, with brighter objects making the 'jump' to higher EW at later times. The small group of outliers below the EW{MgII} mean trend between +5 and +10 days may just be reflecting a slightly brighter group of SNe in the high-*z* sample. The average *s* value within these SNe is just above 1.0 [this corresponds to brighter SNe, see Fig. 9 in Astier *et al.* (2006)], which supports this hypothesis. This feature comparison may be more sensitive to slight differences in the strecth distribution of the samples than the other EW results. Further investigation into this parameter, both observationally and theoretically, is certainly warranted.

5.2. Rate of Peculiar SNe

The EW results of this large high-*z* set note 2 to 3 objects (out of 54 distant supernovae with EW results, $\sim 3-6\%$) that are spectroscopically similar to the class of 1991T-like SNe sub-types that have been observed locally. Previous studies of distant SNe Ia have noted a similarly small percentage of these sub-types in the high-*z* samples; only spectra from SNe 2002iv ($z = 0.231$), 2003jn ($z = 0.33$), 2002fd ($z = 0.27$) (Garavini *et al.* 2007), and 2003lh ($z = 0.56$) (Matheson *et al.* 2005; Krisciunas *et al.* 2005) have been shown to be quantitatively similar to 1991T or 1999aa. This is in contrast to the apparent contribution of these sub-types to the low-*z* SNe sample, which is roughly 10% to 20% (Li *et al.* 2001a; Strolger *et al.* 2002). This has been interpreted as a possible sign of evolution (Branch 2001; Li *et al.* 2001a,b) or of a significant difference between the nearby and distant SNe Ia populations. The identification of the 3 possible 1991T-like objects in this high-*z* sample nearly doubles the number of these sub-types observed at higher redshifts, but the percentage of identified 1991T-like SNe is still much lower than at low-*z*. It is difficult to determine the significance of this apparent discrepancy due to the unknown influence of selection effects. For example, the low-*z* peculiar objects are often singled out for spectroscopic follow up and thus may be over-represented in the nearby sample. Another complication is the uncertainty with regards to whether the overluminous 1991T-like and 1999aa-like SNe are distinct sub-classes of Type Ia SNe or if they represent a possible continuum of thermonuclear SNe (Branch *et al.* 2006). Note that the EW and $v_{\rm ej}$ measurements cannot readily address this latter issue; the overluminous high-*z* objects are referred to as '1991T-like' in the interest of brevity only and does not represent an attempt to clarify the debate on the 1991T-1999aa relationship.

It may be that the difference between the fraction of these sub-types at different redshifts is primarily an effect of the epoch coverage differences between these data sets. SNe 1991T and 1999aa displayed unusual spectroscopic features primarily before maximum light and then evolved to look little different than core normal SNe. Within the low-*z* set considered here, 77% of the SNe were observed at least once prior to maximum light, compared to only 33% (18 of 54 SNe) of the high-*z* sample. With the simple assumption that this factor of ~ 2 difference has reduced the number of overluminous SNe possibly identified in the high-*z* sample by a similar amount, the disparity in the percentage of overluminous sub-type identifications between the two data sets is explained.

Even if this explanation is true, there is still a lack of of the underluminous 1991bg-like SNe at high redshifts. This is perhaps expected for this data set as many factors work against SNLS spectroscopic identification of these objects. Mostly, it is because they are intrinsically much fainter and thus harder to observe photometrically and spectroscopically. This implies that even if the SNLS is observing these objects spectroscopically, they would be much harder to conclusively type. Thus the lack of 1991bg-like SNe Ia in this set is not unexpected.

The end of Sec. 2.1.1 summarizes that, due to the SNLS survey setup, high-*z* SNe with vastly different properties than the nearby objects would most likely not be selected for spectroscopic observation. Thus, the conclusions of the tests made here cannot rule out that such a population of SNe Ia exists at high-*z*, although none of the results show any indication of new subclasses of distant SNe. However, we note that occasionally very rare and unsual objects are found [see SNLS object 03D3bb in Howell *et al.* (2006), for example].

5.3. Implications for Progenitors

Comparisons of SNe Ia across different host galaxy types can also reveal keys to the progenitor scenarios for these objects. One model of SNe Ia formation (Scannapieco & Bildsten 2005) has used the implications of observed SNe Ia environmental dependencies (Wang *et al.* 1997; Umeda *et al.* 1999; Hamuy *et al.* 2000; Howell 2001; Mannucci *et al.* 2005) to create a model that describes SNe Ia as two distinct populations; a 'prompt' component dependent on the galaxy star formation rate and a 'delayed' component whose rate is proportional to galaxy mass. This model has been supported with SNLS data (Sullivan *et al.* 2006) and may be useful in predicting any evolutionary shifts in Sne Ia properties (Howell *et al. in prep*). The measurements made in this study can also be put into the context of this 'two-component' model. Table 5 and Fig 8 show a trend of SiII with host type (at both low and high-*z*) in the direction expected from this two-component model. At all redshifts, SNe in spiral hosts show weaker SiII. Assuming that these early type galaxies are star-forming, and hence host the 'prompt' SNe Ia (which also tend to be the brighter, higher stretch SNe Ia), and that the EW{SiII}-$M_{\rm B}$ correlation is valid, then the trend of lower EW{SiII} measurements in SNe from late type galaxies agrees with the main aspects of the two-component model.

Another implication of this model is that as observations are extended to higher redshifts, a larger sampling of SNe Ia from the 'prompt' star formation-based population would be expected. As these 'prompt' SNe are brighter than their 'delayed' counterparts, this should correspond to additional observations of SNe with high *s* values and correspondingly low EW{SiII} measurements. This effect can be tested in the SNLS sample considered here by combining the high-*z* results from all galaxy types. χ^2 tests and measures of correlation show no statistical difference in EW{SiII} between low and high-*z* samples (see also Fig. 9). However, this could be due to a lack of sensitivity to detect this subtle drift in the population. A possible shift of $\approx 10\%$ in the brightness (or stretch) of the high-*z* population (Howell *et al. in prep*) would correspond to a change of the order of a few (≈ 4) Å in EW{SiII}; Table 5 shows that the error in the means of the distribution of high-*z* EW{SiII} is on the order of this shift and is much higher than the corresponding error in the low-*z* results. An SNLS sample with 2-3 times more SNe (which will be available before the survey is complete) should be able to detect this shift toward the 'prompt' SNe.

6. Conclusions

New results from a quantitative study of a large set of spectra from high-*z* SNe Ia used for cosmological fitting have been compared to corresponding measurements on a sample of SNe Ia observed locally. The measurements from all of the studied high-*z* spectra are within the range of the results at low-*z*. A statistical comparison of these data sets reveals that there is no significant difference (less than 2σ) in the strength of 2 SNe Ia-specific absorption features and the ejection velocity of CaII H&K. The 4th feature – which quantifies absorption from MgII and other ions near 4300 Å – shows a possible difference that should be investigated further.

These methods also reveal a new spectroscopic sequence in SNe Ia based on the strength of the SiII feature near 4000 Å at epochs close to maximum luminosity. An initial test of this sequence was made on a sub-set of 18 SNLS SNe that had the appropriate EW{SiII} measurement and were published with previous SNLS cosmology results (Astier *et al.* 2006). This demonstrated that the EW{SiII}-$M_{\mathrm{B_{peak}}}$ relation reduces the scatter in high-*z* luminosity distance estimates in a manner consistent with the lightcurve shape-luminosity corrections that are currently used to standardise SNe Ia peak magnitudes for cosmology.

At present this type of spectroscopic analysis is one of the most promising avenues of investigating the dispersion, homogeneity and possible evolution of distant Type Ia supernovae. This paper has used empirical techniques on the largest set of distant SNe Ia data studied to date. Although the selection method used to generate the SNLS high-z sample implies that the existence of a new population of Type Ia SNe at high-z with unusual spectral properties cannot be ruled out, a large set of high-*z* SNe have been shown to be spectroscopically similar to nearby objects. At high-z the same trends of SN properties with host type are seen as at low-z, and furthermore, within each host galaxy class no evidence for evolution in SN properties with redshift is seen. These results represent an important step in addressing one of the most pressing issues for Type Ia cosmology.

Acknowledgements. The SNLS collaboration gratefully acknowledges the assistance of Pierre Martin and the CFHT Queued Service Observations team. We also thank the Gemini queue observers and support staff for both taking the data presented in this paper and making observations available quickly. TJB is grateful to Exeter College and the Alberta-Bart Holaday Scholarship. TJB would also like to thank the EU Type Ia SNe RTN 'young researchers' – particularly Gabriele Garavini and Gaston Folatelli – for all of their assistance. Canadian collaboration members acknowledge support from NSERC and CIAR; French collaboration members from CNRS/IN2P3, CNRS/INSU and CEA; Portuguese Collaboration members acknowledge support from FCT-Fundacao para a Ciencia e Tecnologia; UK collaborators acknowledge support from the Science and Technolgy Facilities Council (STFC, formerly PPARC).

SNLS relies on observations with MegaCam, a joint project of CFHT and CEA/DAPNIA, at the Canada-France-Hawaii Telescope which is operated by the National Research Council of Candada, the Institut National des Science de l'Univers of the Centre National de la Recherche Scientifique of France, and the University of Hawaii. This work is based in part on data products produced at the Canadian Astronomy Data Centre as part of the CFHT Legacy Survey, a collaborative project of the National Research Council of Canada and the French Centre national de la recherche scientifique. The Work is also based on observations obtained at the Gemini Observatory, which is operated by the Association of Universities for Research in Astronomy, Inc., under a cooperative agreement with the NSF on behalf of the Gemini partnership: the National Science Foundation (United States), the STFC (United Kingdom), the National Research Council (Canada), CONICYT (Chile), the Australian Research Council (Australia), CNPq (Brazil) and CONICET (Argentina). This research used observations from Gemini program numbers: GN-2005A-Q-11, GN-2005B-Q-7, GN-2006A-Q-7, GS-2005A-Q-11 and GS-2005B-Q-6.

The views expressed in this article are those of the authors and do not reflect the official policy or position of the United States Air Force, Department of Defense, or the U.S. Government.

References

Allen, S.W., Schmidt, R.W., Fabian A.C., 2002, MNRAS, 334, 11
Altavilla, G., Fiorentino, G., Marconi, M., *et al*, 2004 MNRAS, 349, 1344
Anupama, G. C., Sahu, D. K., Jose, J., 2005, A&A, 429, 667
Astier, P., *et al.*, 2006, A&A, 447, 31
Balland, C., *et al.*, 2006, A&A, 445, 387
Barbon, R., Benetti, S., Capellaro, E., *et al.*, 1990, A&A, 237, 79
Baron, E., Bongard, S., Branch, D., *et al.*, 2006, ApJ, 645, 480
Barris, J., et al,. 2004, ApJ, 602, 571
Benetti, S., *et al.* 2004, MNRAS, 348, 261
Benetti, S., *et al.* 2005, ApJ, 623, 1011
Blondin, S., *et al.* 2006, AJ, 131, 1648
Bongard, S., Baron, E., Smadja, G., Branch, D., Hauschchildt, P.H., 2006, *in prep*
Branch, D., 2001, PASP, 113, 169
Branch, D., Dang, L.C., Hall, N., *et al.*, 2006, PASP, 118, 560
Branch, D., Drucker, W., Jeffrey, D.J., 1988, ApJ, 330, L117
Branch, D., *et al.*, 1983, ApJ, 270, 123
Branch, D., Romanishin, W., Baron, E., 1996, ApJ, 465, 73
Branch, D., and van den Bergh, S., 1993, AJ, 105, 2231
Branch, D., *et al.*, 2003, AJ, 126, 1489
Bronder, T.J., 2006, PhD Thesis, Oxford University
Candia, P., *et al.*, 2003, PASP, 115, 277
Capellaro, E., *et al.*, 2001, ApJ, 549, 215
Elias-Rosa, N., *et al.*, 2006, MNRAS, 369, 1880
Filippenko, A.V., *et al.*, 1992a, ApJ, 384, L15
Filippenko, A.V., *et al.*, 1992b, AJ, 104, 1543
Fisher, A., Branch, D., Hoeflich, P., Khokhlov, A., 1995, AJ, 447, L73
Folatelli, G. 2004. PhD Thesis, University of Stockholm
Gallagher J.S., *et al.*, 2005 ApJ, 634, 210
Garavini, G., *et al.*, 2004, AJ, 128, 387
Garavini, G., *et al.*, 2007, *submitted to A&A*
Gibson, B. K., *et al.*, 2000, ApJ, 529, 723
Goldhaber, G., *et al.*, 2001, ApJ, 558, 359
Gomez, G., Lopez, R., 1998, AJ, 115, 1096
Guy, J., Astier, P., Nobili, S., Regnault, N., Pain, R., 2005, A&A, 443, 781
Hachinger, S., Mazzali, P.A., Benetti, S., 2006, MNRAS, 370, 299
Hamuy, M., *et al*, 1996, AJ, 112, 2391
Hamuy, M., *et al.*, 2000, AJ, 120, 1479
Hatano, K., *et al.*, 2000, ApJ, 543, L49
Hillebrandt, W., Niemeyer, J., 2000, ARA&A, 38, 191
Hoeflich, P., Wheeler, J.C., Thielemann, F.K., 1998, ApJ, 495, 617
Hook, I., *et al.*, 2004, PASP, 116, 425
Hook, I., *et al.* 2005, AJ, 130, 2788
Howell, D. A., 2001, ApJ, 554, L193
Howell, D. A., Wang, L., 2002, BAAS, 34, 1256
Howell, D. A., *et al.* 2005, ApJ, 634, 1190
Howell, D. A., *et al.* 2006, Nature, 443, 308
Hsiao, E., *et al.* in press, accepted by ApJ
Jeffrey, D.J., *et al.* 1992 ApJ, 397, 304
Kirshner, R., Jeffery, D., Leibundgut, B., Challis, P.M., Sonneborn, G., 1993, ApJ, 415, 589
Knop, R., *et al.* 2003, ApJ, 598, 102
Krisciunas, K., *et al.*, 2005, AJ, 130, 2453
Leibundgut, B., 2001, ARA&A, 39, 67
Lentz, E.J., Baron, E., Branch, D., 2000, 530, 966
Levan, A., *et al.*, 2005, ApJ, 624, 880
Li, W. D. *et al.*, 1999, AJ, 117, 2709
Li, W., Filippenko, A.V., Riess, A.G., 2001, ApJ, 546, 719
Li, W., Filippenko, A.V., Treffers, R.R., *et al.*, 2001b, ApJ, 546, 734
Mannucci, F., *et al.*, 2005, A&A, 433, 807
Matheson, T., *et al.* 2005, AJ, 129, 2352
Mazzali, P. A., Danziger, I. J., & Turatto, M., 1995, A&A, 297, 509
Mazzali, P., *et al.* 1998 ApJ, 499, L49
Mazzali, P., *et al.* 2005 ApJ, 623, 37
Mazzali, P., Lucy, L.B., Danziger, I.J., 1993, A&A, 269, 423
Nomoto, K., Thielemann, F-K., & Yokoi, K., 1984, ApJ, 286, 644
Nugent, P., Kim, A., Perlmutter, S., 2002, PASP, 114, 803
Nugent, P., *et al.* 1995 ApJ, 455, L147
Patat, F., *et al.*, 1996, MNRAS, 278, 111
Perlmutter, S., *et al.* 1999, ApJ, 517, 565
Phillips, M. M., *et al.* 1987, PASP, 99, 592
Phillips, M. M., *et al.* 1999, AJ, 118, 1766
Reindl, B., Tamman, G.A., Sandage, A., Saha, A., 2005, ApJ, 624, 532
Riess, A.G., Press, W.H., Kirshner, R.P., 1996, ApJ, 473, 88
Riess, A.G., *et al.* 1998, AJ, 116, 1009
Riess, A.G., *et al.* 2004, ApJ, 607, 665
Riess, A.G., *et al.*, 2005, ApJ, 627, 579
Ropke, F.K., Gieseler, M., Travaglio, C., Hillebrandt, W., 2006, A&A, 453, 203
Saha, A., *et al*, 2001, ApJ, 551, 973
Salvo, M.E., *et al.* 2001 MNRAS, 321, 254
Scannapieco, E., & Bildsten, L., 2005, ApJ, 629, L85
Seljak, U., *et al.* 2005, PhRvD, 71, 3515
Spergel, D.N., *et al.* 2006, *in prep.*
Spergel, D.N., et. al. 2003, ApJS, 148, 175

Stern, D., *et al.* 2004, ApJ, 612, 690
Stritzinger, M., *et al.*, 2002, AJ, 124, 2100
Sullivan, M., *et al.* 2003 MNRAS, 340, 1057
Sullivan, M., *et al.* 2006 AJ, 131, 960
Sullivan, M., *et al.* 2006 ApJ, 648, 868
Strolger, L.G., *et al.*, 2002, AJ, 124, 2905
Travaglio, C., Hillebrandt, W., & M. Reinecke, 2005, A&A, 443, 1007
Tully, R.B., *Nearby Host Galaxies Catalogue*, Cambridgue University Press, Cambridge, UK
Turatto, M., *et al.*, 1996, MNRAS, 283, 1
Turatto, M., *et al.*, 1998, AJ, 116, 2431
Umeda, H., Nomoto, K., Kobayashi, C., Hachisu, I., Kato, M., 1999, ApJ, 522, L43
Wang, L., Hoeflich, P., Wheeler J.C., 1997, ApJ, 483, 29
Wells, L.A., *et al.*, 1994, AJ, 108, 2233
Yamaoka, H., Nomoto, K., Shigeyama, T., Thielemann, F.K., 1992, ApJ, 393, L55

Table 6. Observed properties and instrument settings for SNLS SNe candidates observed from November 2004 to May 2006. The magnitudes and “percentage increase” are estimated from the lightcurves and correspond to the date of spectroscopy.

SN Name	RA (2000)	Dec (2000)	UT Date	Exposure (s)	Mode	$\lambda_{\rm cent}$	seeing (“)	Mag (i’)	$\%_{\rm inc}$
04D1pu	02:27:28.437	-04:44:41.71	2004-12-12	7200	N&S	720	0.49	24.08	39
04D2mh	09:59:45.872	+02:08:27.94	2005-01-09	2400	C	720	1.00	22.90	730
04D2mj	10:00:36.535	+02:34:37.44	2005-01-09	3600	N&S	720	0.62	23.19	54
05D1az	02:25:12.492	-04:36:08.17	2005-09-04	5400	N&S	720	0.63	23.78	1246
05D1by	02:24:35.448	-04:12:04.16	2005-09-03	5400	N&S	720	0.62	23.56	9
05D1bz	02:25:00.685	-04:12:00.74	2005-09-02	7200	N&S	720	0.88	23.96	4310
05D1cc	02:26:31.173	-04:09:53.40	2005-09-05	3600	N&S	720	0.46	23.18	114
			2005-09-06	1800			0.83	23.18	114
05D1ee	02:24:46.766	-04:00:01.86	2005-10-31	3600	N&S	720	0.59	23.24	25
05D1ej	02:26:06.317	-04:43:45.79	2005-10-27	3600	N&S	720	0.47	22.83	15
05D1em	02:24:05.503	-04:56:23.35	2005-11-05	3600	N&S	720	0.62	23.71	476
			2005-11-06	1800			0.57	23.71	9524
05D1eo	02:25:23.116	-04:38:33.36	2005-10-27	5400	N&S	720	0.39	23.75	21
05D1er	02:25:41.466	-04:00:16.32	2005-10-28	7200	N&S	720	0.55	23.99	94
05D1hn	02:24:36.254	-04:10:54.94	2005-12-04	2700	C	680	0.63	20.86	249
05D1ju	02:26:57.303	-04:08:02.78	2005-12-27	7200	N&S	720	0.50	24.04	91
05D1ka	02:24:58.945	-04:34:28.56	2005-12-28	5400	N&S	720	0.86	23.21	1059
05D1kl	02:24:33.544	-04:19:08.33	2005-12-31	5400	N&S	720	0.59	23.61	247
05D2ab	10:01:50.833	+02:06:23.02	2005-01-09	1800	C	680	0.67	21.83	263
05D2ah	10:01:28.704	+01:51:46.18	2005-01-09	1800	C	680	0.96	20.83	1017
05D2ck	10:00:45.203	+02:34:22.13	2005-02-16	5400	N&S	720	0.65	23.88	7592
05D2ja	10:00:03.809	+02:17:36.12	2005-05-07	5400	C	680	0.94	22.15	115
05D2nt	10:00:58.234	+02:22:21.62	2005-12-26	5400	N&S	720	0.69	23.46	340
05D2ob	09:59:00.705	+01:50:56.62	2005-12-28	5400	N&S	720	0.73	24.22	242
05D3ax	14:19:17.595	+52:41:15.07	2005-02-11	5400	N&S	720	0.45	23.40	342
05D3bt	14:18:35.980	+52:54:55.95	2005-03-06	3600	C	720	0.84	23.52	71
05D3cf	14:16:53.369	+52:20:42.47	2005-03-08	3600	C	720	0.69	22.96	94
05D3ci	14:21:48.085	+52:26:43.33	2005-03-09	5400	N&S	720	0.76	23.03	70
05D3cq	14:18:46.173	+53:07:55.55	2005-04-11	5400	N&S	720	0.64	24.10	156
05D3cx	14:21:06.560	+52:45:01.70	2005-04-09	5400	N&S	720	0.50	23.52	65
05D3jq	14:21:45.462	+53:01:47.53	2005-06-04	5400	N&S	720	0.60	23.36	30
05D3ki	14:21:16.341	+52:35:42.47	2005-05-14	5400	N&S	720	0.67	23.68	49
05D3km	14:22:38.298	+53:04:01.14	2005-06-04	5400	N&S	720	1.0	23.89	536
05D3kp	14:20:02.952	+52:16:15.28	2005-06-03	5400	N&S	720	0.81	23.36	7848
05D3kt	14:19:53.730	+52:44:34.64	2005-06-03	5400	N&S	720	0.82	23.53	141
05D3lb	14:17:31.775	+53:10:04.38	2005-06-05	5400	N&S	720	0.51	23.38	192
05D3lc	14:22:22.902	+52:28:44.11	2005-06-06	3600	C	720	0.63	22.67	17
05D3lw	14:17:44.021	+53:06:24.98	2005-07-01	7200	N&S	720	0.45	24.41	170
05D3mn	14:18:45.206	+52:19:23.56	2005-07-12	7200	N&S	720	0.77	23.31	77
05D3mh	14:18:59.805	+52:40:03.50	2005-07-10	7200	N&S	720	0.54	23.50	30
05D3mq	14:19:00.398	+52:23:06.81	2005-08-03	1800	C	680	0.71	21.48	4748
05D3mx	14:22:09.078	+52:13:09.35	2005-07-30	2700	C	680	0.83	23.10	>10000
05D3ne	14:21:02.946	+52:29:43.92	2005-07-14	2700	C	680	0.85	20.48	1074
05D4av	22:14:10.515	-17:54:42.67	2005-07-10	3600	N&S	720	0.53	23.2	77
05D4bm	22:17:04.621	-17:40:39.45	2005-07-11	3600	C	680	0.55	22.04	144
05D4ca	22:14:11.350	-17:48:15.47	2005-08-02	2700	C	720	0.63	22.24	156
05D4cn	22:13:31.454	-17:17:19.92	2005-08-02	5400	N&S	720	0.70	23.30	82
05D4dt	22:14:25.851	-17:40:16.03	2005-09-02	3600	N&S	720	0.55	22.62	20
05D4dx	22:13:39.387	-18:03:20.99	2005-09-06	5400	N&S	720	0.47	23.14	39
05D4dy	22:15:30.102	-18:12:55.54	2005-09-06	5400	N&S	720	0.53	23.87	684
05D4fn	22:17:01.076	-17:49:25.16	2005-10-08	7200	N&S	720	0.65	23.86	4474
05D4fo	22:15:20.925	-17:16:05.25	2005-10-07	3600	N&S	720	0.77	22.47	1845
05D4gw	22:14:47.365	-17:31:54.99	2005-11-05	5400	N&S	720	0.46	23.69	283
05D4hn	22:17:13.545	-17:54:45.40	2005-12-01	5400	N&S	720	0.50	23.50	474
06D3bz	14:17:10.044	+53:01:29.31	2006-02-08	3600	N&S	720	0.71	23.20	115
06D3cb	14:20:43.536	+52:11:28.11	2006-02-03	5400	N&S	720	0.88	23.61	213
06D3cc	14:17:31.604	+52:54:44.79	2006-02-02	5400	N&S	720	0.58	23.55	99
06D3cl	14:22:15.106	+52:16:41.53	2006-03-06	5400	N&S	720	0.61	23.75	264
06D3cn	14:19:25.826	+52:38:27.78	2006-03-06	1800	C	680	0.40	21.26	372
06D3du	14:21:18.563	+53:03:27.10	2006-05-24	5400	N&S	720	0.45	24.27	54

Table 6. continued.

SN Name	RA (2000)	Dec (2000)	UT Date	Exposure (s)	Mode	$\lambda_{\rm cent}$	seeing (“)	Mag (i’)	$\%_{\rm inc}$
06D3dz	14:18:14.731	+52:56:23.11	2006-05-02	2400	C	680	0.98	22.19	66

Table 7. SNLS identifications and derived properties for SNe candidates observed from Nov. 2004 to May 2006.

SN	z	σ_z^{a}	CI & Type[b]	Template[c]	z from[d]
04D1pu	0.639	0.001	3 - SN Ia*	...	OII
04D2mh	0.59	0.01	3 - SN Ia*	1996X +2	SN
04D2mj	0.513	0.001	5 - SN Ia	1992A -1	OII, Hβ, OIII
05D1az	0.842	0.001	5 - SN Ia	1996X +2	possible OII
05D1by	0.298	0.001	5 - SN Ia	2002bo -1	Hα, Hβ, OIII, SII
05D1bz	...	...	2 - SN	...	...
05D1cc	0.564	0.001	5 - SN Ia	1996X +7	Hβ, OII, OIII
05D1ee	0.558	0.001	4 - SN Ia	1992A +6	H&K
05D1ej	0.312	0.001	4 - SN Ia	1989B -5	NII
05D1em	0.866	0.001	5 - SN Ia	1999ee +5	nearby galaxy
05D1eo	0.737	0.001	2 - SN	...	H&K, OII
05D1er	0.85	0.01	3 - SN Ia*	1999aa -1	SN
05D1hn	0.149	0.001	5 - SN Ia	2003du -7	Hα, SII, OII
05D1ju	0.707	0.001	3 - SN Ia*	1996X +7	OII, OIII
05D1ka	0.857	0.001	2 - SN	...	H&K
05D1kl	0.560	0.001	3 - SN Ia*	1990N -7	OII, OII
05D2ab	0.323	0.001	5 - SN Ia	1998bu -4	Hα
05D2ah	0.184	0.001	5 - SN Ia	1994D -5	Hα, SII
05D2ck	0.698	0.001	5 - SN Ia	1992A +6	H&K
05D2ja	0.303	0.001	5 - SN Ia	1999aw +16	Hα, SII, OIII
05D2nt	0.757	0.001	4 - SN Ia	1999ee +3	OII,Hβ, OIII
05D2ob	0.924	0.001	4 - SN Ia	1989B -1	OII
05D3ax	0.643	0.001	5 - SN Ia	1999aw +12	OII, OIII
05D3bt	0.462	0.001	2 - SN	...	Hβ, OII, OIII
05D3cf	0.419	0.001	4 - SN Ia	1999be +19	Hβ, OII, OIII
05D3ci	0.515	0.001	5 - SN Ia	1992A -5	OII, H&K
05D3cq	0.890	0.001	3 - SN Ia*	1999ao +5	Hβ, OII
05D3cx	0.805	0.001	4 - SN Ia	1999bk +7	possible OII
05D3jq	0.579	0.001	4 - SN Ia	2000E +5	Hβ, Hγ, OII
05D3ki	0.965	0.001	2 - SN	...	OII
05D3km	0.97	0.01	3 - SN Ia*	1999bo +1	SN
05D3kp	...	...	2 - SN	...	...
05D3kt	0.648	0.001	5 - SN Ia	1999ee -2	Hβ, OII, OIII
05D3lb	0.647	0.001	5 - SN Ia	1999ee 0	Hβ, OII, OIII
05D3lc	0.461	0.001	3 - SN	...	H&K
05D3lw	0.601	0.001	2 - SN	...	OII
05D3mn	0.760	0.001	3 - SN Ia*	1999av +2	possible OII
05D3mh	0.67	0.01	4 - SN Ia	1998aq -8	SN
05D3mq	0.246	0.001	5 - SN Ia	1992A +9	Hα
05D3mx	0.46	0.01	4 - SN Ia	1998bu +8	SN
05D3ne	0.169	0.001	5 - SN Ia	1994D -4	SDSS host spectrum
05D4av	0.509	0.001	3 - SN Ia*	2002bo -4	OII
05D4bm	0.375	0.001	5 - SN Ia	1996X -1	Hβ, OII, OIII
05D4ca	0.607	0.001	2 - SN	1988A +3	Hβ, OII, OIII
05D4cn	0.763	0.001	3 - SN Ia*	2002bo -1	OII, H&K
05D4dt	0.407	0.001	4 - SN Ia	1994D -2	Hα,OII, H&K, Hβ, OIII
05D4dx	0.793	0.001	3 - SN Ia*	1002A +5	H&K, Hδ
05D4dy	0.79	0.01	4 - SN Ia	1994D +2	SN
05D4fn	0.4	0.1	2 - SN	...	SN
05D4fo	0.373	0.001	5 - SN	1994D -2	Hα, H&K
05D4gw	0.808	0.001	5 - SN Ia	1999bp -2	OII
05D4hn	0.842	0.001	4 - SN Ia	1981B 0	OII, OIII
06D3bz	0.72	0.01	4 - SN Ia	1989B -1	SN
06D3cb	...	...	2 - SN	...	...
06D3cc	0.90	0.01	3 - SN Ia*	1990N -7	...
06D3cl	0.555	0.001	2 - SN	...	OII,OIII,Hβ
06D3cn	0.818	0.001	5 - SN Ia	1996X -1	OII,OIII,Hβ
06D3du	1.0	0.1	2 - SN	...	SN
06D3dz	0.294	0.001	2 - SN	...	Hα,SII

continued on next page

Table 7. continued.

SN	z	σ_z^{a}	CI & Type[b]	Template[c]	z from[d]

a — redshifts identified with host galaxy features are accurate to ≈ ±0.001; redshifts identified with template matches are accurate to ≈ ±0.01

b — final object identification and confidence index

c — best low-z spectral fit (name and days past max.)

d — the host features used to estimate z

Appendix A: Results - Spectroscopic analysis of SNLS SNe Ia

Table A.3. Equivalent width and ejection velocity results for the published high redshift SNe Ia observed by the SNLS at the Gemini telescopes. This set includes all of the SNLS objects (reduced by the author) that were confirmed as Type Ia SNe (a confidence index of 3 or higher) and were subject to less than 65% contamination from their host galaxies. The blank spaces (‘· · ·’) indicate where a measurement had to be removed due to inadequate wavelength coverage. The uncertainties in the EW results include measurement errors, errors from any possible variance in the pseudo-continuum, and the uncertainty from the host galaxy contamination correction.

Name	Day^{a*}	EW{CaII}^{b*}	EW{SiII}^{b*}	EW{MgII}^{b*}	$v_{ej}^{c*}/1000.0$
03D1ax	-2.30 (0.11)	117.6(15.4)	13.8(2.0)	105.3(10.0)	11.84(0.29)
03D1bk	-5.23 (0.25)	95.7(11.6)	21.0(3.7)	98.3(18.2)	12.71(3.40)
03D1cm	-4.42 (0.59)	52.0(13.1)	14.8(10.6)	125.0(27.5)	16.98(1.81)
03D1co	7.42 (0.44)	87.8(16.9)	16.7(3.4)	246.2(21.8)	13.99(6.45)
03D1ew	1.53 (0.91)	144.2(19.5)	23.5(12.7)	83.2(26.4)	20.21(1.32)
03D4cj	-8.05 (0.01)	· · ·	5.9(6.1)	131.6(13.8)	· · ·
03D4cn	0.53 (2.42)	116.9(16.0)	17.0(5.4)	76.0(12.3)	13.85(1.14)
03D4cy	5.86 (0.59)	163.2(22.5)	8.7(5.8)	124.5(35.3)	16.38(3.22)
03D4fd	-0.88 (0.70)	100.2(14.3)	21.4(5.2)	79.4(16.4)	14.83(0.45)
03D4gl	8.27 (0.28)	104.8(16.6)	17.0(5.3)	72.9(10.4)	20.42(1.96)
04D1de	-6.80 (0.10)	91.4(14.5)	9.4(1.3)	105.1(12.9)	20.78(1.01)
04D1hd	1.85 (0.04)	· · ·	11.9(11.5)	99.1(21.4)	15.25(1.44)
04D1hy	-2.19 (0.44)	· · ·	15.5(6.0)	101.4(16.9)	16.11(2.05)
04D1ow	6.28 (0.42)	139.0(14.9)	21.1(10.2)	92.7(22.4)	14.66(3.02)
04D2ae	-1.95 (1.78)	· · ·	13.1(7.5)	128.4(18.7)	19.41(1.87)
04D2mh	1.58 (0.24)	116.5(29.1)	18.2(11.9)	· · ·	14.41(5.15)
04D3dd	3.68 (1.69)	109.5(19.8)	30.7(15.9)	· · ·	16.97(1.42)
04D3fq	1.35 (0.66)	83.3(23.4)	26.6(10.2)	102.5(26.2)	16.26(2.76)
04D3kr	5.37 (0.09)	· · ·	15.8(1.8)	118.0(11.6)	14.43(1.63)
04D3lp	1.00 (0.20)	100.1(16.9)	· · ·	· · ·	17.62(2.28)
04D3mk	-1.47 (0.55)	· · ·	2.2(1.0)	129.0(15.4)	12.31(2.08)
04D3ml	-0.89 (0.84)	96.8(11.6)	· · ·	138.9(25.3)	13.06(1.53)
04D3nq	9.36 (0.04)	· · ·	· · ·	154.5(34.8)	· · ·
04D3ny	2.15 (0.67)	· · ·	26.9(7.4)	91.3(18.8)	11.23(4.32)
04D4dm	3.55 (0.47)	· · ·	9.7(4.9)	120.6(24.5)	18.56(2.50)
04D4hu	6.22 (0.29)	68.6(11.2)	12.9(3.0)	· · ·	· · ·
04D4ic	2.92 (0.66)	· · ·	17.7(7.9)	137.0(21.3)	15.92(1.69)
04D4ii	-4.58 (0.34)	· · ·	10.7(3.9)	122.2(15.3)	19.99(3.21)
04D4jy	2.00 (0.40)	73.9(24.8)	· · ·	· · ·	15.34(1.48)
05D1az	8.85 (0.17)	75.6(13.5)	8.9(7.0)	102.1(17.5)	14.13(0.15)
05D1cc	6.80 (0.15)	89.7(17.9)	· · ·	102.0(11.8)	12.79(0.58)
05D1em	6.69 (0.23)	126.8(17.7)	25.0(16.5)	140.9(34.2)	14.95(2.76)
05D1er	2.83 (0.42)	· · ·	29.0(5.5)	160.7(18.9)	16.35(1.83)
05D1ju	6.28 (0.27)	163.2(24.6)	13.2(3.6)	116.50(15.7)	18.46(2.79)
05D1kl	-4.27 (0.21)	97.0(17.0)	7.6(5.3)	100.8(14.9)	18.92(3.56)
05D2ab	-1.30 (0.08)	· · ·	13.8(7.5)	93.5(11.3)	15.34(3.64)
05D2ah	-2.49 (0.03)	· · ·	10.2(10.4)	92.0(21.0)	· · ·
05D2ck	0.730 (0.74)	71.5(24.7)	24.4(8.3)	148.7(24.0)	14.07(0.36)
05D2ja	9.63 (0.12)	· · ·	· · ·	161.3(25.3)	· · ·
05D3ax	8.03 (0.39)	118.9(9.0)	· · ·	65.6(7.2)	14.77(0.62)
05D3cf	13.68 (0.41)	· · ·	· · ·	273.1(44.1)	· · ·
05D3cq	11.6 (1.35)	106.9(23.1)	· · ·	· · ·	13.51(0.32)
05D3cx	10.28 (0.61)	· · ·	27.2(5.7)	98.5(13.6)	10.01(0.33)
05D3km	1.46 (0.31)	87.1(19.7)	· · ·	· · ·	13.67(2.07)
05D3kt	-3.86 (0.30)	· · ·	· · ·	123.5(15.2)	18.34(2.68)
05D3lb	-1.21 (0.24)	· · ·	9.2(2.6)	88.5(7.7)	19.16(1.35)
05D3mh	2.71 (0.40)	96.4(22.1)	25.6(4.6)	154.3(21.5)	13.43(1.79)
05D3mn	2.82 (0.40)	80.7(25.7)	14.8(3.7)	136.4(14.7)	13.88(0.24)
05D3mq	8.45 (0.07)	· · ·	3.6(15.1)	232.8(35.2)	· · ·
05D4av	5.84 (0.15)	· · ·	9.3(6.7)	54.1(9.5)	· · ·
05D4bm	-3.81 (0.05)	162.0(14.3)	14.5(2.9)	85.7(7.8)	19.98(0.99)
05D4cn	0.39 (0.32)	62.3(10.7)	18.2(4.3)	146.2(13.2)	14.10(0.57)
05D4dy	2.13 (0.55)	· · ·	23.2(6.6)	127.1(19.2)	11.33(2.50)
05D4gw	0.13 (0.34)	162.6(22.1)	16.8(5.9)	115.8(13.8)	18.70(2.08)
05D4fo	-5.31 (0.03)	· · ·	28.6 (5.1)	82.6 (11.7)	· · ·

continued on next page

Table A.3. continued.

Name	Day[a*]	EW{CaII}[b*]	EW{SiII}[b*]	EW{MgII}[b*]	$v_{\rm ej}^{c*}/1000.0$

a — Rest-frame day, relative to B' max
b — Equivalent Width, Å
c — Ejection velocity, km/s
***** 1σ *errors listed in parentheses*

Online Material

Appendix B: SNLS Observed Spectra

Sprectra from each Supernova Legacy Survey SN candidate observed at the Gemini telescopes from December 2004 through May 2006. The observed properties and observation setup for each object is summarized in Table 6 and the final object identifications and redshift estimates are displayed in Table 7. These spectra have been corrected for sky absorption, the narrow host galaxy features have been removed, and the GMOS chip gaps have been interpolated over. These images show the observed spectrum, re-binned to 7.5 Å resolution, in dark blue with a smoothed version of the spectrum overplot in light blue. The smoothed spectrum is for illustrative purposes only and was generated witha Savitsky-Golay filter computed with a 3$^{\text{rd}}$ degree polynomial fit over 40 pixels of the observed spectrum. Note that for some of these spectra a large amount of host galaxy contamination is clear.

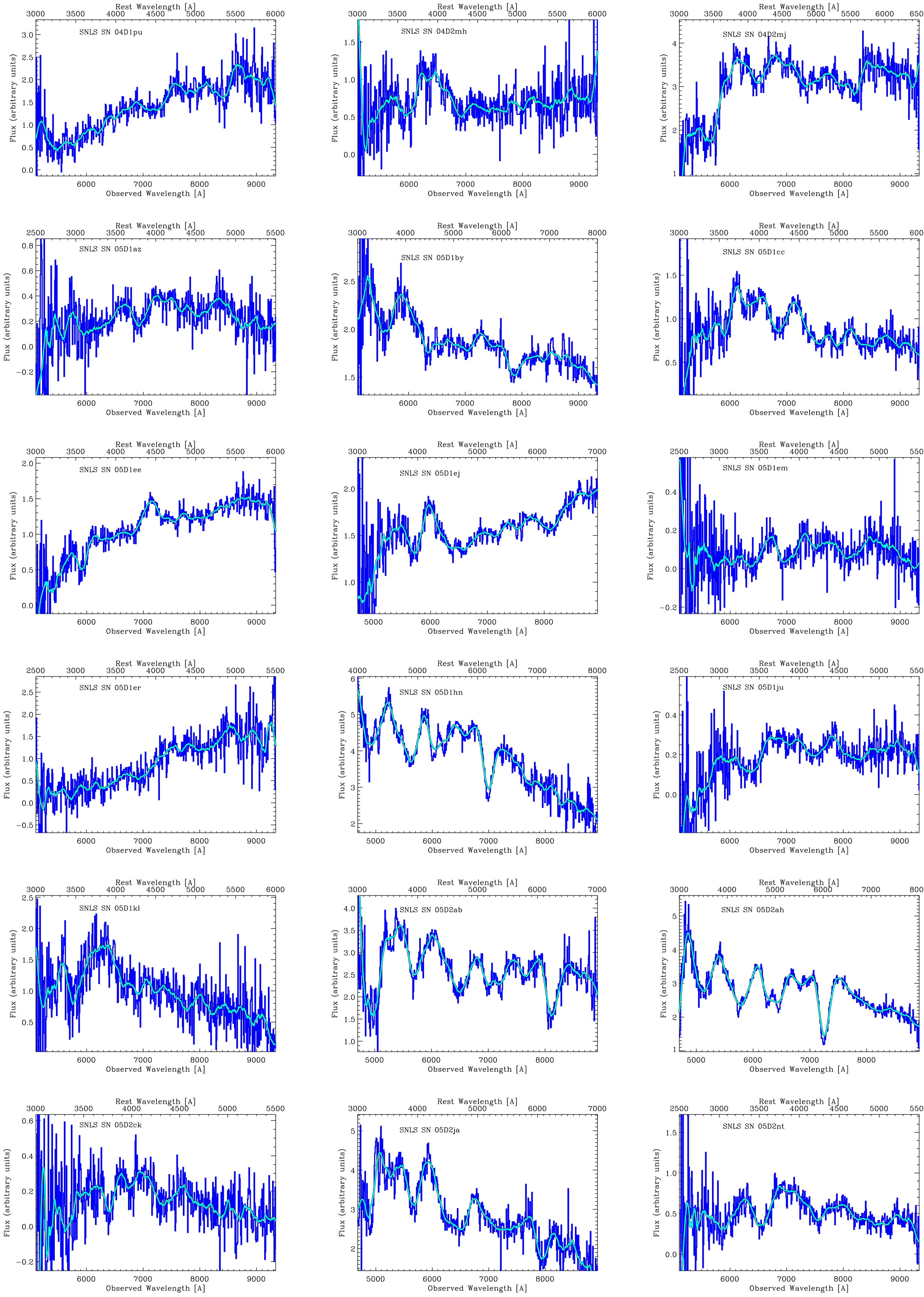

Fig. B.1. Confirmed SNe Ia. The observed, re-binned spectrum is shown in dark blue and the smoothed spectrum is overplot in light blue for illustrative purposes.

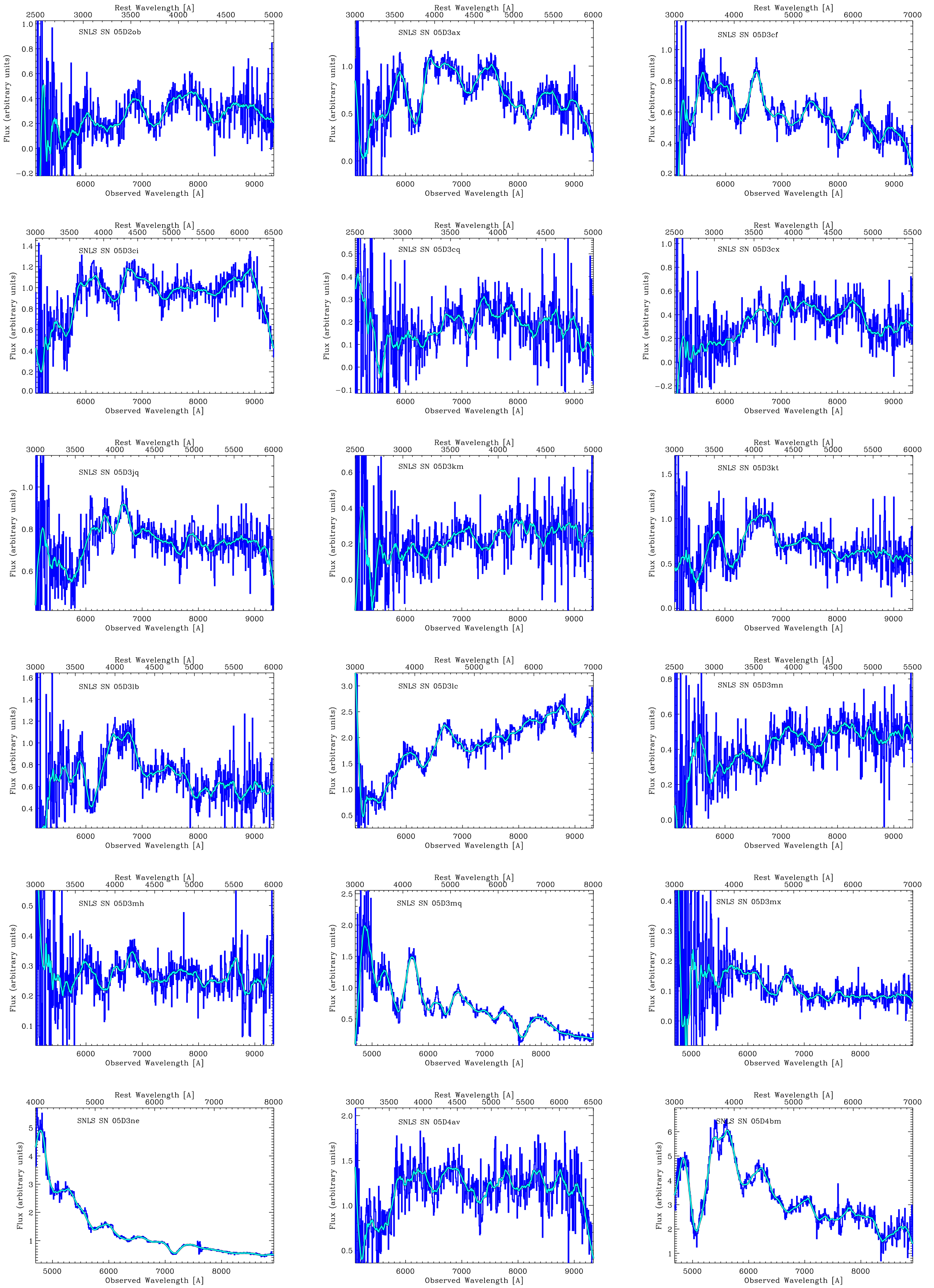

Fig. B.2. Confirmed SNe Ia. The observed, re-binned spectrum is shown in dark blue and the smoothed spectrum is overplot in light blue for illustrative purposes.

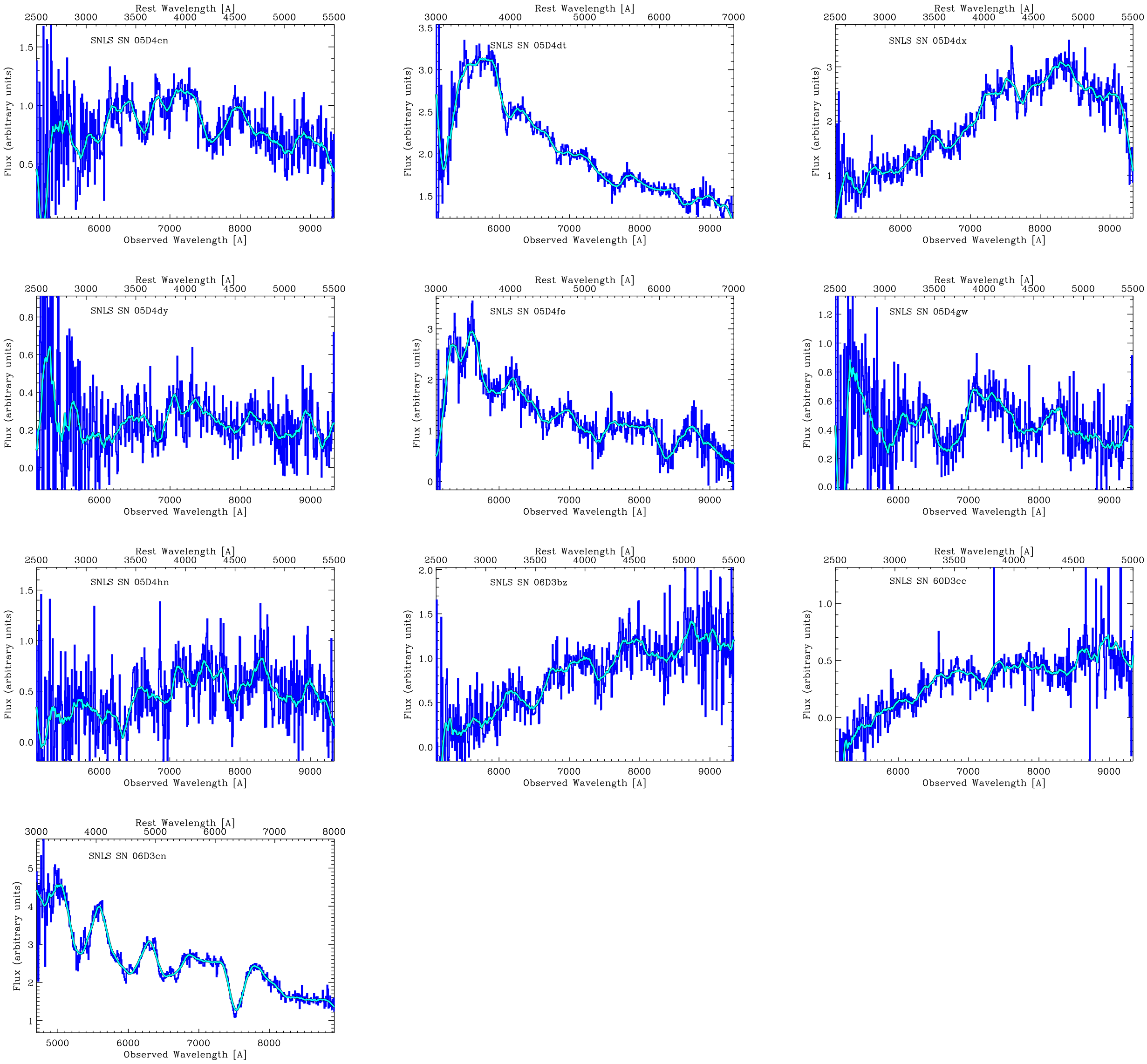

Fig. B.3. Confirmed SNe Ia. The observed, re-binned spectrum is shown in dark blue and the smoothed spectrum is overplot in light blue for illustrative purposes.

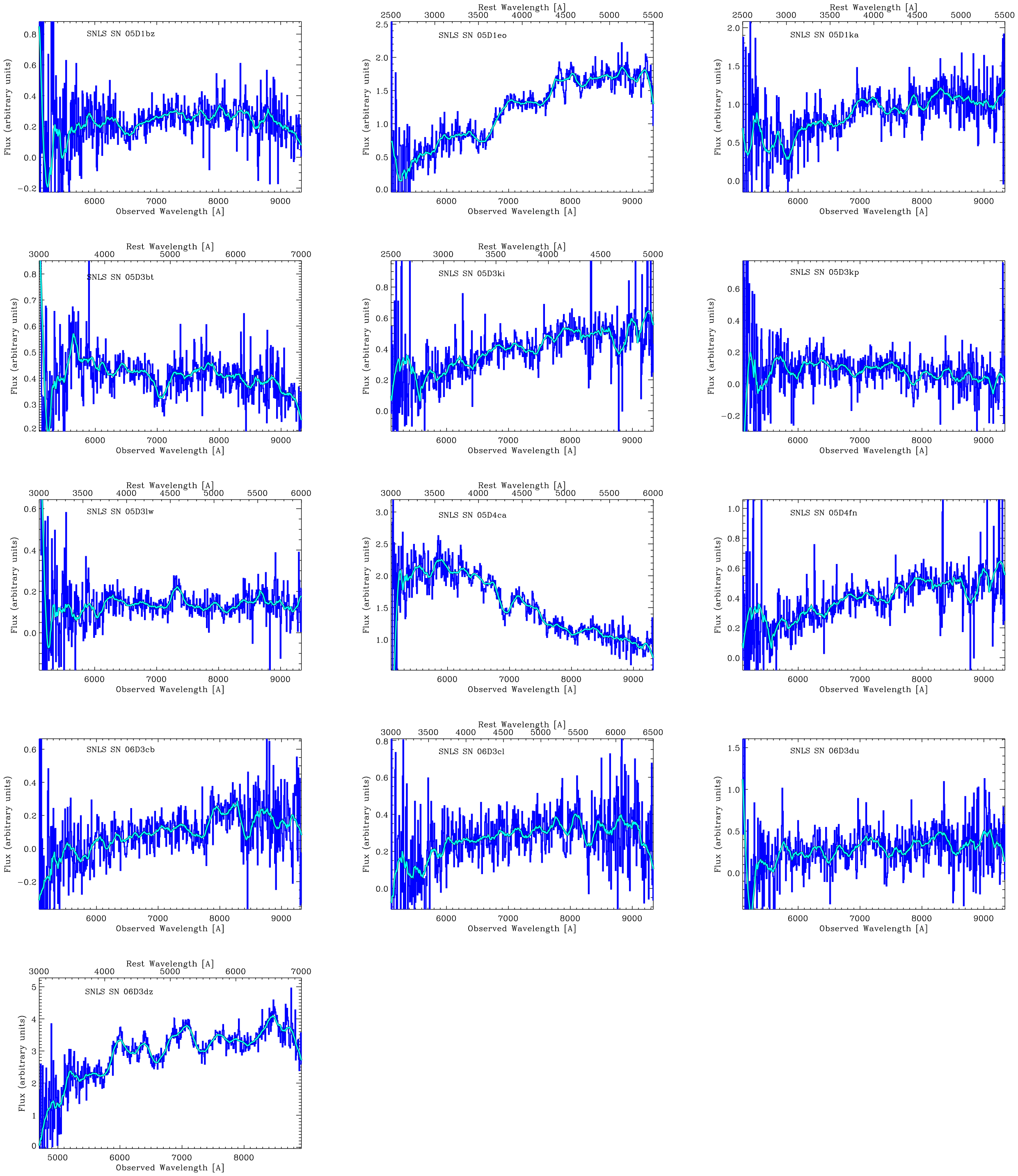

Fig. B.4. Unidentified SN candidates. The observed, re-binned spectrum is shown in dark blue and the smoothed spectrum is overplot in light blue for illustrative purposes.